Mineralium Deposita
https://doi.org/10.1007/s00126-024-01300-4

ARTICLE

Unraveling the evolution of the Bodó W-skarn district in the Seridó Mineral Province (NE-Brazil): constraints from C-O stable isotopes, thermodynamic modeling, and geochronology

Dinarte Lucas[1] · Maria Helena B. M. Hollanda[1] · João Adauto de Souza Neto[2] · Renato Moraes[1] · Laécio Cunha de Souza[3]

Received: 28 December 2023 / Accepted: 16 July 2024

Abstract

Tungsten mineralization in the Bodó mineral district (9 Mt with an average grade of 2% WO_3) is in a sequence of metasomatized marbles and W-(Mo)-skarn lenses in the Seridó Belt, northern Borborema Province. The marble lenses have variable amounts of diopside, grossular, scapolite, phlogopite, and tremolite. The skarn lenses are mainly composed of massive grossular, diopside, vesuvianite, epidote, and quartz. A spatially related granite yielded a SHRIMP U–Pb zircon date of 536.6 ± 3.4 Ma and a $^{40}Ar/^{39}Ar$ biotite date of 490.65 ± 0.67 Ma, whereas a nearby pegmatite yielded a $^{40}Ar/^{39}Ar$ muscovite date of 501.63 ± 0.59 Ma. Literature data for molybdenite in the skarn mineralization yielded a Re–Os date of 510 ± 2 Ma, which is coeval with U–Pb dates of columbite-tantalite from other regional pegmatites (515–509 Ma). Therefore, it is likely that pegmatite magmatism acted as the source of fluid and heat for the mineralization. The C–O stable isotope data for marbles and skarns are consistent with interaction of magmatic fluid and host marble at variable XCO_2 conditions. T-XCO_2 pseudosections define peak conditions of metamorphism/metasomatism at 650–600 °C over a wide range of XCO_2 (between 0.4 and 0.8), whereas the retrograde stage started at ~550 °C. Late garnet crystallization at low XCO_2 (< 0.2) indicates high H_2O influx, while scapolite crystallization required high XCO_2 (~0.8). Together with the interpretation of textural relationships, these observations indicate that skarn and marble formation occurred under open-system conditions with fluctuating XCO_2 fluid composition as a consequence of magmatic fluid infiltration.

Keywords Borborema Province · Seridó Mineral Province · Skarn · Phase equilibrium modeling · C-O stable isotopes

Introduction

Skarn deposits are important sources of metals such as W, Au, Fe, Cu, Zn, Mo, and Sn. These rocks are complex and form by magmatic fluids interacting with reactive Ca-(Mg)-rich country rocks, leading to the development of unique calc–silicate mineral assemblages (Zharikov 1970; Einaudi et al. 1981). The process of skarn formation involves the metasomatic addition of various components from an igneous source, such as Cl, F, Fe, W, S, Si, and Al. The formation of the metasomatic mineral assemblage is controlled by the variation of CO_2 in the magmatic fluid coupled with other parameters such as temperature, pressure, fluid chemistry, and protolith composition (Korzhinskii 1968; Kwak 1987; Robb 2005; Lefebvre et al. 2019a, b; Romer et al. 2022). Nevertheless, some authors have recently been discussing the formation of skarn during regional metamorphism (e.g. the Hämmerlein skarn deposit; Lefebvre et al. 2019a, b; Romer et al. 2022). In this scenario, skarn formation is linked to the peak regional metamorphism of a pre-enriched sedimentary protolith, and mineralization is a result of

Editorial handling: L. Torró

✉ Dinarte Lucas
dinarte@usp.br

[1] Instituto de Geociências, Universidade de São Paulo, São Paulo, SP 05508-080, Brazil

[2] Departamento de Geologia, Universidade Federal de Pernambuco, Recife, PE 50740-530, Brazil

[3] Departamento de Geologia, Universidade Federal do Rio Grande do Norte, Natal, RN 59078-970, Brazil

Published online: 27 July 2024

metal remobilization due to the subsequent emplacement of granites.

The Borborema Province embraces a major metallogenetic region known as the Seridó Mineral Province (Fig. 1a). The Seridó Mineral Province contains W–(Mo)–(Au) skarn deposits (Souza Neto et al. 2008), mineralized pegmatites with Nb–Ta–(Li), rare earth elements (REEs), and gems such as Paraíba tourmaline (Beurlen et al. 2008, 2014), as well as other mineralization styles including mafic–ultramafic-hosted emerald (Santiago et al. 2019; Araújo Neto et al. 2023), orogenic Au (Araújo et al. 2002), and banded Fe formations (Sial et al. 2015; Cavalcante et al. 2016). The Seridó Mineral Province features more than 700 skarn occurrences in an area of approximately 20,000 km² (Santos

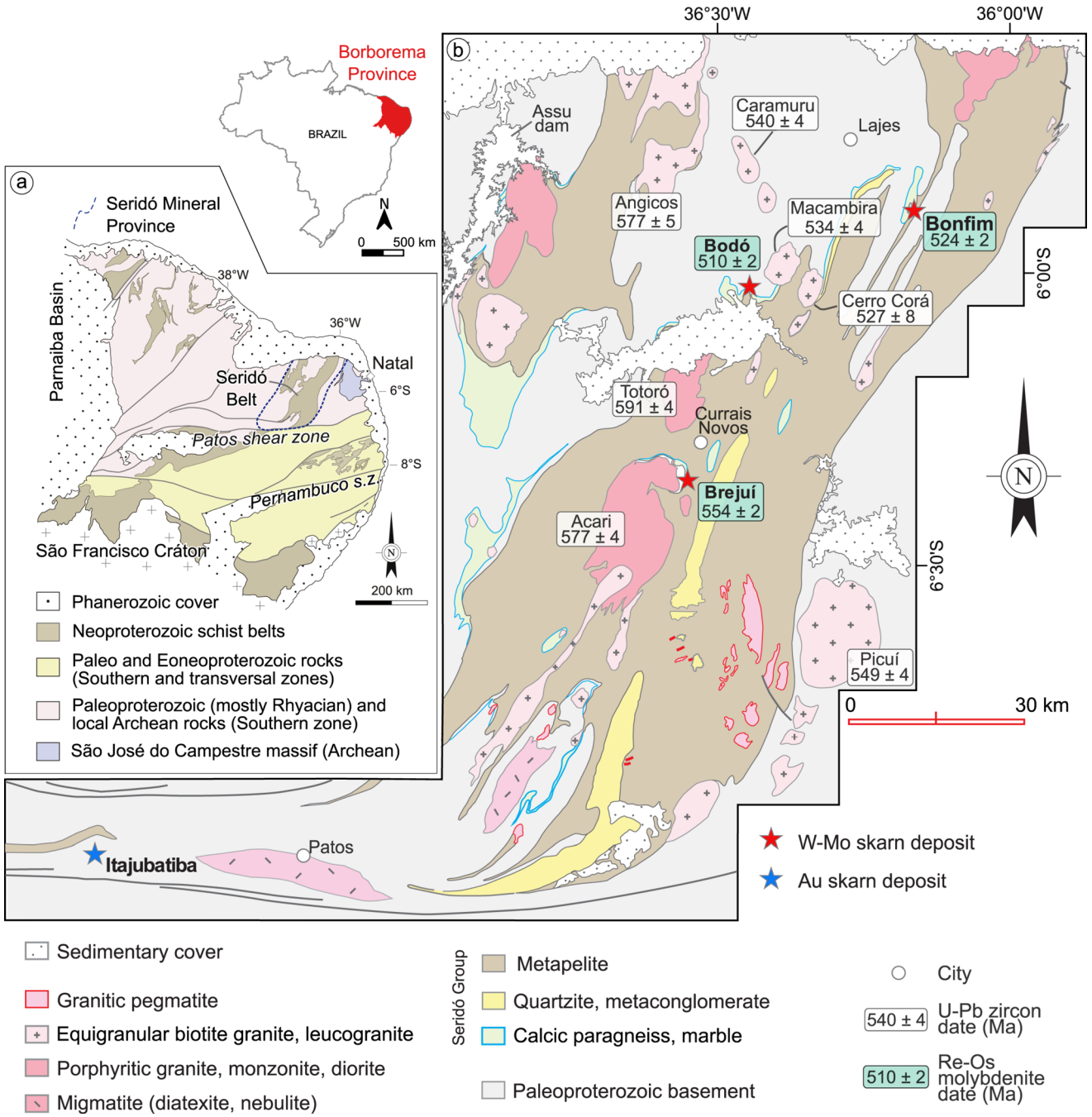

Fig. 1 (**a**) Geological setting of the Borborema Province in northeastern Brazil highlighting the Seridó Mineral Province (modified from Hollanda et al. 2017). (**b**) Simplified geological map of the Seridó belt modified from Hollanda et al. (2017) showing the location of the main skarn deposits. Ages for granitic magmatism from Caramuru, Angicos, Cerro Corá and Picuí are from Hollanda et al. (2017); Acari and Totoró dates are from Archanjo et al. (2013); Macambira date is from this study. Re–Os dates for the mineralization are from Hollanda et al. (2017)

et al. 2014). Tungsten exploration in the province has been developed since the 1940s and approximately 60,000 tons of WO_3 have been produced (Souza Neto et al. 2008).

Three skarn deposits stand out in the Seridó Mineral Province: Bodó, Brejuí, and Bonfim. The Bodó mine is located in the homonymous district, a 12-km-long belt where a few minor W-skarn occurrences are also present (Fig. 2). The Bodó deposit is currently the highest-grade tungsten mine in the Seridó Mineral Province, with ore reserves estimated at 9 Mt at a grade of 2% WO_3. The Bonfim and Brejuí ore reserves are estimated at 5 and 11 Mt, respectively, sharing average grades of 0.5-1.0% WO_3 (Santos et al. 2014). Tungsten is the main product in most skarn bodies, with Mo and, in particular, Au as important by-products, with the exception of the Itajubatiba skarn deposit, in which Au is the only metal exploited (Souza Neto et al. 1998, 2008).

Skarns and pegmatites have historically been genetically linked to the late Ediacaran–Cambrian granitic magmatism that extensively intruded along the Seridó Belt (Silva et al. 1995; Souza Neto et al. 2008; Santos et al. 2014). This connection is due to their close spatial relations, and it is assumed that high-K calc-alkaline granitic magmas were the fluid source for skarn formation. Additionally, the late crystallization of granitic magmas is believed to have played a role in the emplacement of granitic pegmatites. Nevertheless, Re–Os dating of molybdenite from the three main deposits (Brejuí, Bonfim, and Bodó) in the Seridó Mineral Province (Hollanda et al. 2017) and available U–Pb zircon (ca. 600 – 526 Ma), U-Pb columbite-tantalite (ID-TIMS dates of ca. 515 – 509 Ma), and $^{40}Ar/^{39}Ar$ mica (ca. 520 – 500 Ma) data from granites and granitic pegmatites (Araújo et al. 2005; Baumgartner et al. 2006; Archanjo et al. 2013; Hollanda et al. 2015, 2017; Souza et al. 2016; Strmić Palinkaš et al. 2019) have so far failed to establish a link between magmatism and skarn formation, as the ages of the deposits do not match those of nearby igneous bodies.

The objective of this study is to investigate the geological processes and geochemical conditions that lead to the formation of W-skarn mineralization in the Bodó mineral district. Thus, we aim to elucidate the general principles governing the formation of such mineral deposits, providing insights that can be applied to unravel the source of

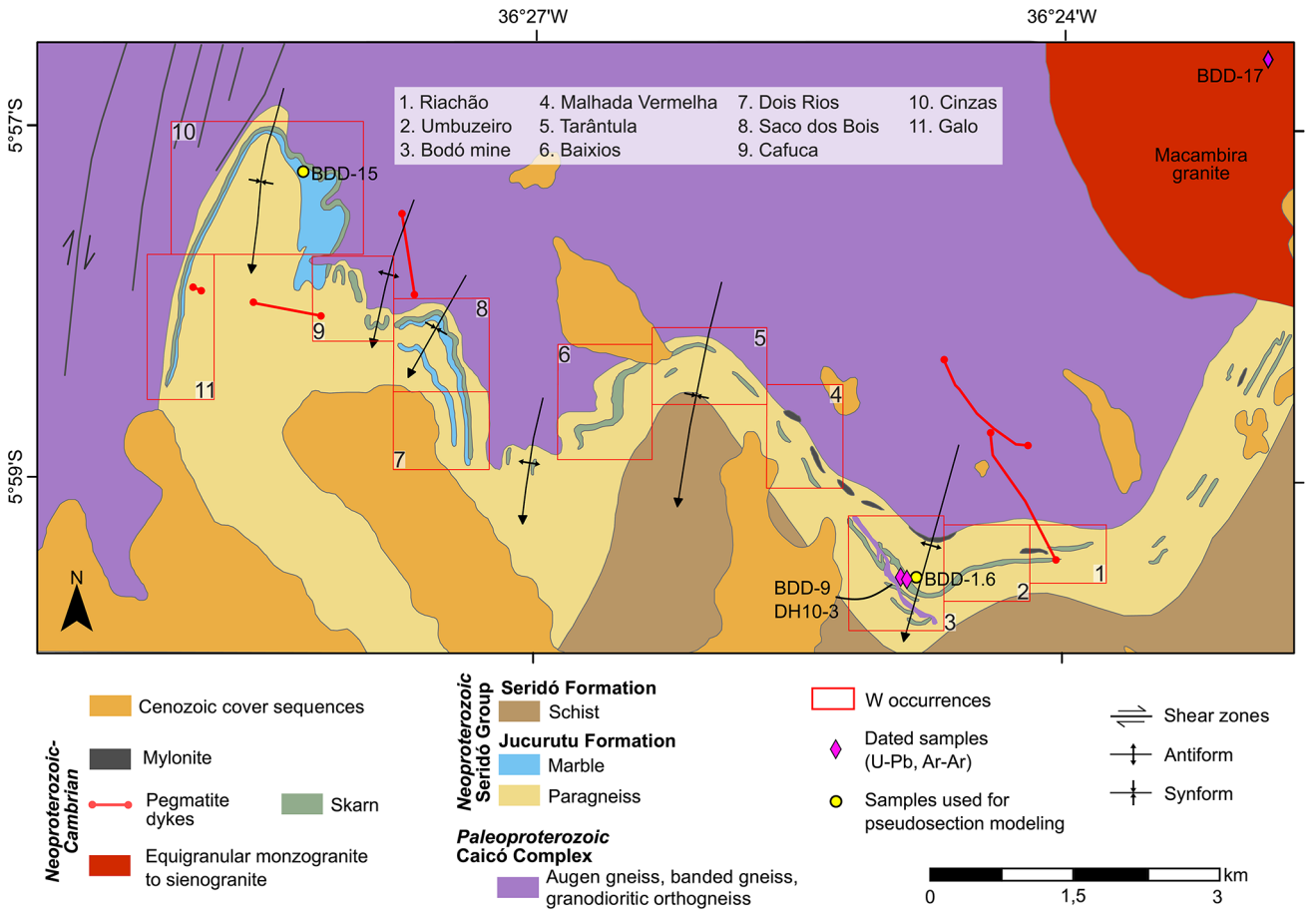

Fig. 2 Geological map highlighting the regional-scale folding system that controlled the W–Mo mineralization in the Bodó district. Sampling locations (BDD-17 for U–Pb dating; BDD-17, BDD-9, and DH10-3 for $^{40}Ar/^{39}Ar$ dating; BDD-1.6, BDD-15 for thermodynamic modeling), as well as major W-skarn occurrences in the Bodó district are indicated

fluids related to skarn formation and the metamorphic and metasomatic evolution of skarn deposits. With this in mind, we investigate the potential connection between skarn mineralization and magmatic-fluid sources via geochronology of a nearby granite pluton and granitic pegmatite. We also present carbon and oxygen isotope data to model the role of magmatic fluids during the metasomatism of marbles and the genesis of the skarns in the Bodó district. Lithogeochemical and mineral chemistry data were used to construct T-XCO_2 pseudosections to constrain the prevailing metamorphic/metasomatic conditions during the evolution of the magmatic-hydrothermal system.

Geological setting

The Borborema Province and the Seridó Belt

The Borborema Province in northeastern Brazil (Almeida et al. 1981) is a complex geologic terrain formed during the assembly of the Western Gondwana. The province underwent significant deformation, metamorphism, and magmatism during the Brasiliano orogeny in the Neoproterozoic (Brito Neves et al. 2000; Ganade de Araujo et al. 2014; Caxito et al. 2020, 2021). The amalgamation of Gondwana during the Neoproterozoic resulted in the formation of a continental-scale transcurrent shear zone system (Vauchez et al. 1995; Archanjo et al. 2021; Fossen et al. 2022). The major E-W-trending Patos and Pernambuco shear zones divide the Borborema Province in three tectonic sub-provinces or domains: Northern, Southern, and Transversal (or Central) (Brito Neves et al. 2000; Van Schmus et al. 2011; Oliveira and Medeiros 2018).

The Archean and Paleoproterozoic cratonic nuclei of the Borborema Province are overlain by Neoproterozoic mobile belts. The Seridó Belt is a NE-trending metasedimentary sequence located in the northern portion of the province. It was deposited in the Ediacaran period and later deformed in the Brasiliano orogeny (625–510 Ma; Caxito et al. 2020). The tectonic setting is characterized by dextral transpressive deformation, where NE-trending shear zones are interconnected with the regional Patos shear zone (Corsini et al. 1991; Archanjo et al. 2013).

The Seridó Group (Fig. 1b) is an Ediacaran terrigenous sedimentary sequence unconformably deposited over an Archean–Paleoproterozoic migmatite–gneiss basement (Dantas et al. 2004, 2013; Hollanda et al. 2011; Souza et al. 2016; Ferreira et al. 2020). The Jucurutu Formation of the Seridó Group is characterized by paragneiss with marble lenses of meters to tens of meters in length and minor felsic–intermediate meta-volcanic rocks, mica schist and, subordinately, quartzite lenses (Caby et al. 1995; Van Schmus et al. 2003), and meter-thick layers of banded iron formation (BIF) (Sial et al. 2015). The Jucurutu paragneiss grades laterally and upward to a thick, turbidite-like sequence consisting dominantly of mica schist of the Seridó Formation with minor marble and calc-silicate lenses (Caby et al. 1995; Jardim de Sá et al. 1995; Van Schmus et al. 2003). Neodymium isotope data indicate that the transition between the Jucurutu and the Seridó formations was gradational and conformable, with increasingly radiogenic compositions toward the top. Youngest detrital zircon dates indicate that the deposition of the Seridó Group occurred during the early Ediacaran, at ca. 650–610 Ma (Van Schmus et al. 2003; Hollanda et al. 2015). The intrusion of granite-diorite plutons in the metapelites of the Seridó Formation occurred after ca. 597 Ma (e.g., Totoró pluton; Archanjo et al. 2013; Hollanda et al. 2015, 2017). This indicates that the deposition of the entire succession ceased before 600 Ma, with the distal Seridó Formation overlapping the platformal graywacke–carbonate–BIF association of the Jucurutu Formation during a marine transgression.

At the base of the Seridó Group lies the Equador Formation, which is made up of quartzite and oligomictic to polymictic metaconglomerate. This formation is laterally discontinuous and assigned to an intermediate stratigraphic position between the Jucurutu and Seridó formations (Caby et al. 1995; Jardim de Sá et al. 1995; Van Schmus et al. 2003). A recent study on the detrital zircon provenance of the Seridó Group showed no zircons younger than 1.8 Ga in the quartzite or metaconglomerate of the Equador Formation and strongly negative ε_{Nd} zircon values (< -22.0). These data differ from the values of the Jucurutu–Seridó succession which provided abundant Neoproterozoic zircon dates and ε_{Nd} from −11.0 to -4.5 (Hollanda et al. 2015). The oldest detrital zircon of the Jucurutu Formation coincides with those of the regional basement rocks, whereas in the Seridó-Jucurutu sequence detrital zircons indicate a prominent Neoproterozoic source. Thus, this change in sedimentary provenance may indicate a regional unconformity between the deposition of the Equador sedimentary rocks and the other units (Hollanda et al. 2015).

The metamorphic conditions of the Seridó paleobasin reached 620 °C and 2.5-4.0 kbar (Lima 1987, 1992; Souza 1996; Souza et al. 2007; Cioffi et al. 2021), with locally higher temperatures near the granitic intrusions. The emplacement of granitoids and diorites in the Seridó Belt was related to voluminous felsic to mafic magmatism emplaced during the pre- to post-collisional stages of the Brasiliano orogeny (Archanjo et al. 2013). According to their geochemical affinities, these rocks can be divided into (i) shoshonitic (K-rich) gabbro and diorite, (ii) high-K oxidized calc-alkaline granite (*s.l.*) with grain sizes and textures varying from porphyritic to medium-grained equigranular,

and (iii) A-type quartz syenite and syenogranite (Jardim de Sá 1994; Nascimento et al. 2015). Minor occurrences of calc-alkaline granite and charnockite complete the geochemical diversity of the Brasiliano magmatism in the northeastern Borborema Province. U-Pb ages range from 597 to 525 Ma (Archanjo et al. 2013; Souza et al. 2016; Hollanda et al. 2017). Later granitic pegmatite dikes and sills intruded supracrustal rocks of the Seridó Group (Silva et al. 1995; Beurlen et al. 2008, 2014, 2019). ID-TIMS U–Pb columbite-tantalite dates constrain their emplacement to the Cambrian period, mostly at ca. 515–509 Ma (Baumgartner et al. 2006), whereas U–Pb dates on monazite and $^{40}Ar/^{39}Ar$ dates on muscovite extend this interval to ca. 525–502 Ma (Araújo et al. 2005; Baumgartner et al. 2006; Beurlen et al. 2008; Strmić Palinkaš et al. 2019).

Skarns and W–Mo–Au mineralization in the Seridó Mineral Province

The major skarns from the Seridó Mineral Province (Brejuí, Bonfim, and Bodó) are centimeter- to meter-thick stratabound deposits developed within the marble or along the lithologic contact between the marble and paragneiss of the Jucurutu Formation (Souza Neto et al. 2008). Although these deposits do not strictly share the same mineral assemblage, they encompass prograde and retrograde metasomatic assemblages, and a later phase of Fe–Cu and Bi–Te ± Au mineralization. The prograde mineral assemblage is defined by diopside–grossular–plagioclase ± amphibole (the latter can also be a retrograde phase), whereas the retrograde mineral assemblage includes epidote, clinozoisite, vesuvianite, and zeolite (Souza Neto et al. 2008; Santos et al. 2014). The main ore minerals are scheelite and molybdenite, with minor pyrite and chalcopyrite in Brejuí and Bodó. In the Bonfim deposit, the W–Mo–Au mineralization is associated with bismuthinite, bismite, native bismuth, joseite, chalcopyrite, and sphalerite. In contrast, in the Itajubatiba deposit native gold is often associated with pyrrhotite, chalcopyrite, pyrite, and magnetite (Souza Neto et al. 2008, 2012). Re–Os molybdenite dates provided Ediacaran–Cambrian ages for the mineralization in Brejuí (ca. 554 Ma), Bonfim (ca. 524 Ma), and Bodó (ca. 510 Hollanda et al. 2017).

The Bodó mine is centered on one of several marble lenses deformed along a sequence of NE-trending anticline–syncline fold systems developed due to syn-Brasiliano transpressional kinematics (Fig. 2). Locally, skarns and hydrothermally modified marble lie stratigraphically in contact with the Jucurutu paragneiss. A few igneous bodies are exposed around the mine area. A fine-grained biotite leucogranite shows incipient solid-state foliation and abundant pegmatite and aplite dikes of varying width are mapped on the surface and underground. The Macambira granite is a subcircular body exposed a few kilometers to the northeast. This granite is a K-rich calc-alkaline pluton in which biotite syenogranite and monzogranite are the prevailing facies (Silva and Souza 2012).

Sampling and analytical methods

The samples were collected from a variety of locations within the Bodó district to ensure that the data reflected the overall characteristics of skarn and marble as accurately as possible. In the Bodó mine, samples were collected from outcrops, drill cores, and accessible mine galleries. At the other skarn occurrences, samples were collected only from outcrops. A summary of the analyzed samples can be found in ESM Table S1.

U-Pb zircon and $^{40}Ar/^{39}Ar$ mica geochronology

The geochronologic investigation targeted (i) one representative sample of the Macambira pluton for U–Pb (zircon) and $^{40}Ar/^{39}Ar$ (biotite) dating; (ii) a granitic pegmatite dike in the Bodó mine area collected for $^{40}Ar/^{39}Ar$ (muscovite) dating; and (iii) a mylonite collected for $^{40}Ar/^{39}Ar$ (muscovite) dating. A graphical representation of the drill cores investigated is provided in ESM Fig. S1.

Zircons were extracted from the bulk rock samples by conventional hydraulic, magnetic, and density separation (heavy liquids), then handpicked, mounted, and polished, and finally imaged in transmitted light and on a scanning electron microscope in cathodoluminescence (CL) mode. U–Pb isotope analyses were performed on the SHRIMP IIe hosted at the Institute of Geosciences, University of São Paulo (Brazil). The reader is referred to Sato et al. (2014) for details of the instrumentation and data acquisition and reduction. The isotopic ratios of U and Pb of the unknown samples and the TEMORA standard (Black et al. 2003, 2004) were measured in sets of six mass scans, with TEMORA being analyzed after every third unknown analysis. The standard provided a concordia age of 416.8 ± 1.4 Ma (2σ, $n = 18$, MSWD = 0.035). U, Th, and Pb abundances and Pb isotope ratios were normalized to the SL13 zircon standard (U = 238 ppm). Common Pb correction was performed using the measured ^{204}Pb and assuming the Pb isotope composition after Stacey and Kramers (1975) model. Raw data were reduced using SQUID 2.5, and U-Pb dates were calculated using IsoplotR v5.2 software (Vermeesch 2018). Uncertainties on the calculated concordia dates are reported at 1σ confidence level. The complete U–Pb dataset is provided in ESM Table S2.

Mica concentrates from samples and Fish Canyon sanidine standard were irradiated for 14 h in the CLICIT facility of the TRIGA reactor at Oregon State University (USA).

After radioactive cooling, mica grains and standards were loaded onto a Cu disk, sealed in a 10^{-10} vacuum chamber, and heated under increasing temperature steps using a Nd-YVO_4 laser (532 nm) connected to an ARGUS VI (Thermo Scientific) mass spectrometer at the Isotope Geology Center (https://uspmulti.prp.usp.br/centrais/dashboard/122), Institute of Geosciences, University of São Paulo. Corrections for the instrumental blank were made simultaneously with the data acquisition. Data visualization, corrections for nuclear interference, mass discrimination, and irradiation parameter J, as well as date calculation were performed with ArArCALC v2.6 (Koppers 2002) and IsoplotR (Vermeesch 2018). The $^{40}Ar/^{39}Ar$ data are provided in ESM Table S3.

Bulk-rock, mineral, and isotope geochemistry

The bulk geochemical compositions of two impure marble samples were obtained for use in pseudosection analyses. They were collected at sites BBD-1.6 and BDD-15 in the Bodó mine area and in the Cinzas occurrence, respectively (Fig. 2). These samples were also analyzed for mineral chemistry, together with three skarn samples collected at site BDD-22 and along drill core DDH-10. A powder aliquot of 30 g obtained from a 5×5-cm fragment of rock was fused with lithium tetraborate and analyzed for major element compositions by X-ray fluorescence spectrometry using the facilities of the Technological Characterization Laboratory (https://uspmulti.prp.usp.br/public/centrais/4) at the Department of Mining and Petroleum Engineering, University of São Paulo. The loss on ignition (LOI) was estimated from the weight difference after ignition of 2 g of rock at 1020 °C. The complete bulk-rock analyses are reported in ESM Table S4.

Back-scattered electron (BSE) images were taken using a Variable Pressure Environmental Scanning Electron Microscope (VPESEM) Quanta 250 model coupled to an Oxford Energy Dispersive X-ray Spectrometer (EDS) at the Institute of Geosciences, University of São Paulo. The thin sections were uncoated, and the imaging conditions were an acceleration voltage of 20 kV, a working distance of 10 mm, a beam size of 5 µm, and a low pressure of 60 Pa.

Mineral chemistry of amphibole, calcite, clinopyroxene, epidote, feldspar, garnet, and scapolite were performed on 30 µm-thick carbon-coated thin sections by wavelength dispersive spectrometry (WDS) on the JEOL JXA-FE-8530 electron microprobe of the Geoanalítica Center (https://uspmulti.prp.usp.br/public/centrais/74) of the Institute of Geosciences, University of São Paulo. The analyses were performed at 15 kV acceleration voltage and a 20 nA beam current, with a beam size of 5 µm. Analytical parameters and calibration standards used for WDS analyses are listed in ESM Table S5.

Finally, carbon and oxygen isotope analyses were obtained from ca. 200 mg bulk aliquots of 44 agate-milled calcite samples from marbles and skarns. The samples were reacted with 100% H_3PO_4 at 72 °C under a He-rich atmosphere in a GasBench II device coupled to a DeltaPlus Advanced (Thermo Scientific) isotope ratio mass spectrometer at the Isotope Geology Center (https://uspmulti.prp.usp.br/centrais/dashboard/124), Institute of Geosciences, University of São Paulo. $\delta^{18}O$ and $\delta^{13}C$ data were measured in reference to the V-PDB (Vienna – Pee Dee Belemnite) standard and stated errors were 0.05‰ and 0.07‰, respectively. $\delta^{18}O$ V-PDB was converted to $\delta^{18}O$ V-SMOW (Vienna Standard Mean Ocean Water) using the equation $\delta^{18}O\ V\text{-}SMOW = 1.03091 * \delta^{18}O\ V\text{-}PDB + 30.91$ (Coplen et al. 1983). The complete C-O isotope data are reported in ESM Table S6.

Thermodynamic modeling

T-XCO_2 pseudosections were constructed using Perple_X 6.9.1 (Connolly 1990, 2009) with the internally consistent thermodynamic dataset tc-ds55, and Holland and Powell's (1998; revised 2004) equation of state for H_2O–CO_2. Sample BDD-15 was modeled in the NKCFMAS-HC system, whereas sample BDD-1.6 was modeled in the CFMAS-HC system. For the sample BDD-15, Fe^{3+} was ignored because the its content allocated due to the charge balance in the structural formula in the observed mineral assemblage was insignificant. However, the O_2 content in sample BDD-1.6 was estimated to account for the presence of Fe^{3+} in the analyzed garnets. The bulk composition was adjusted through charge balance to generate garnet with the calculated andradite content.

Both T-XCO_2 pseudosections were calculated for fluid-saturated conditions using the following solid solutions: amphibole (Diener et al. 2007), biotite (Tajčmanová et al. 2009), clinopyroxene (Holland and Powell 1998), dolomite (Holland and Powell 1998), calcite (Anovitz and Essene 1987), garnet (White et al. 2000), plagioclase (Newton et al. 1980), and scapolite (Kuhn 2005).

Results

Petrography and mineral chemistry

Bodó district marbles

The Bodó district comprises several discontinuous marble lenses and skarn occurrences and deposits following the sequence of the fold system. The marble occurs in different colors, such as gray, white, green, and orange, and is

characterized by a massive (Fig. 3a-c) or incipient to well-developed foliation (Fig. 3d-e). The marble lenses exhibit heterogeneous mineralogy with some parts mostly composed of carbonates and others with substantial enrichment in silicate minerals representing up to 15% vol. (Fig. 3a, e).

The main mineral assemblage in marbles is diverse and includes amphibole, clinopyroxene, garnet, phlogopite, and scapolite, with smaller amounts of epidote, magnetite, plagioclase, titanite, and wollastonite. Among them, epidote, garnet, scapolite, titanite, and wollastonite are characteristic of the metasomatic stage. The composition of amphibole, calcite, clinopyroxene, epidote, garnet, phlogopite, plagioclase, and scapolite is shown in ESM Table S7.

Calcite is almost pure in composition, nearly equigranular, and displays a coarse-grained mosaic texture. Mica is often aligned, although it does not always show prominent foliation (Fig. 4a-b). It has a uniform phlogopitic composition (X_{Mg} between 0.866 and 0.893). Clinopyroxene occurs

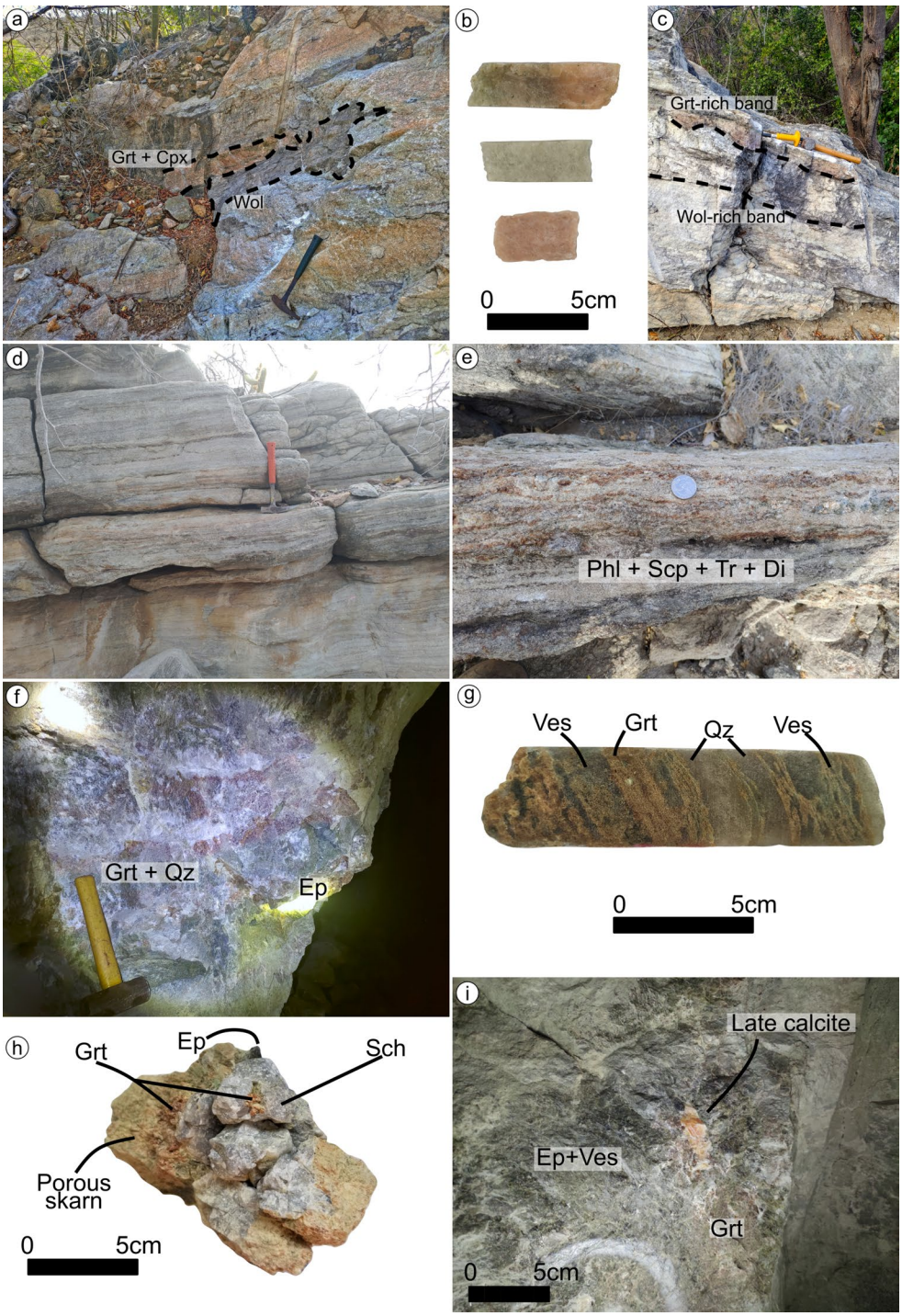

Fig. 3 Marbles (**a**-**e**) and skarns (**f**-**i**) from the Bodó district. (**a**) Greenish and orange marble at the surface of the Bodó mine. Wollastonite and discontinuous/irregularly shaped garnet + clinopyroxene bands. (**b**) Color varieties of massive marbles. Samples BDM11-1, BDM11-4, and BDM4-6, respectively. (**c**) Gray marble from the same outcrop as the marble from Fig. 4a with wollastonite and garnet-rich bands. (**d**) Marble with pervasive foliation from the Cinzas lens with phlogopite and minor diopside. (**e**) Foliated marble with phlogopite, scapolite, tremolite and diopside from the same lens as in Fig. 4d. (**f**) Massive skarn consisting mainly of garnet, quartz, and late epidote. (**g**) Banded skarn composed of garnet, vesuvianite and quartz. (**h**) Porous skarn consisting mainly of altered garnet and epidote, showing large grayish scheelite crystals. Sample BD-4. (**i**) Retrograde skarn composed mainly of epidote and vesuvianite with late orange calcite vugs developed over prograde skarns containing garnet. Sample BDD-N409-1. Abbreviations: Cpx = clinopyroxene, Ep = epidote, Grt = garnet, Phl = phlogopite, Qz = quartz, Scp = scapolite, Sch = scheelite, Ves = vesuvianite, Wol = wollastonite

as individual crystals or as aggregates and may show inclusions of calcite, quartz, and phlogopite (Fig. 4b-c). It is classified as diopside ($Di_{79-92}Hd_{7-21}Jo_{0-1}$, with X_{Mg} ranging from 0.791 to 0.929; ESM Fig. S2a). Amphibole often presents a decussate texture with inclusions of calcite and rarely phlogopite and diopside (Fig. 4d). It can also occur included in diopside. The amphibole is classified as tremolite and shows high X_{Mg} values ranging from 0.900 to 0.969 (ESM Fig. S2b). Epidote forms medium- to coarse-grained xenoblastic crystals around diopside and garnet (Fig. 4e).

Garnet commonly exhibits xenoblastic to hypidioblastic textures with inclusions of calcite and quartz and is often in contact with or partially includes diopside (Fig. 4f). It has a high grossular component (Gr_{70-84}) and

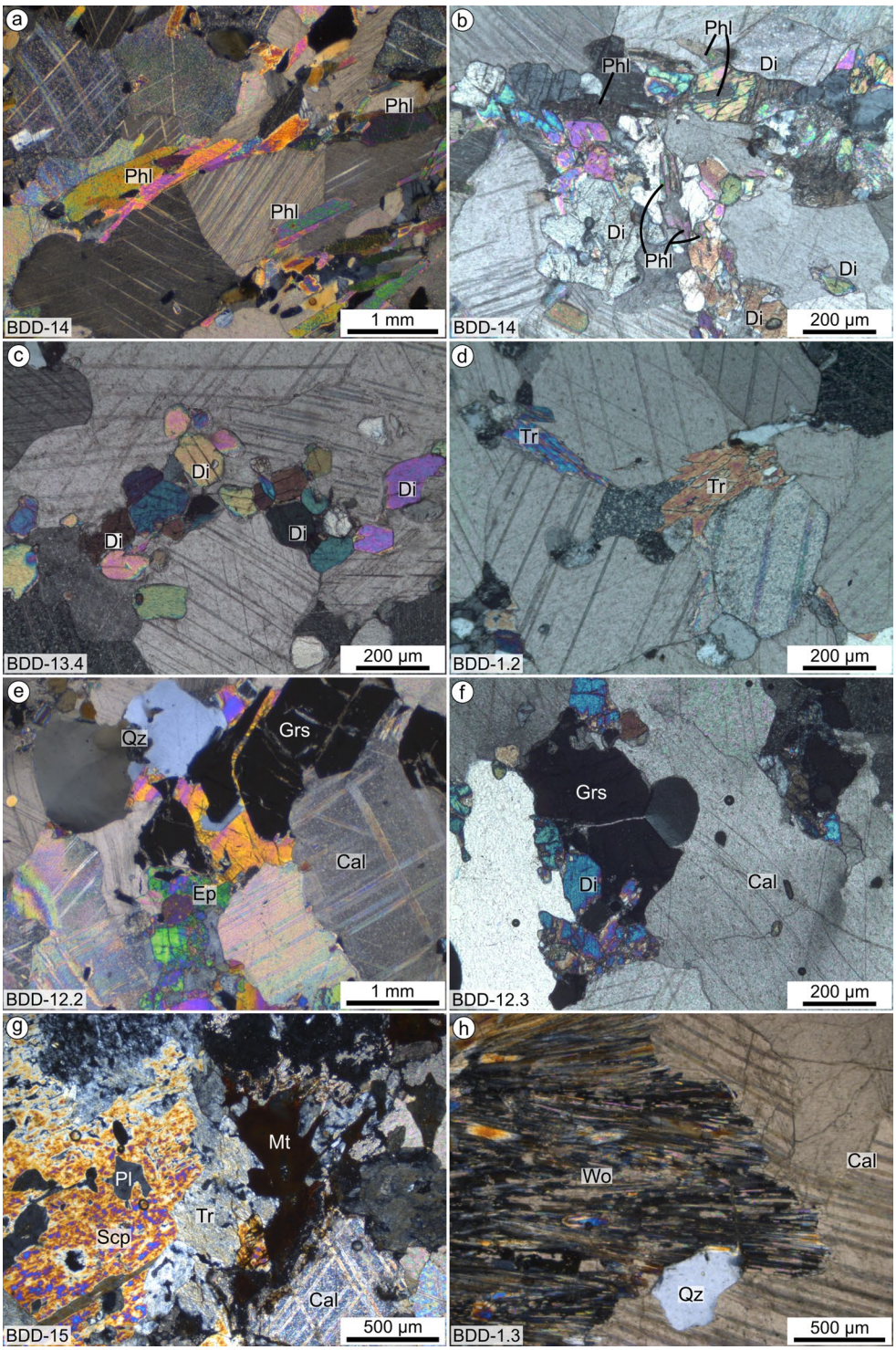

Fig. 4 Photomicrographs of marbles from the Bodó district showing the occurrence of the main silicate phases. (**a**) Crystals of phlogopite in equilibrium with calcite. (**b**) Diopside in contact with and including phlogopite crystals. (**c**) Small-grained crystals of diopside. (**d**) Tremolite between calcite crystals. (**e**) Garnet is replaced by interstitial epidote. (**f**) Garnet encompassing diopside crystals. (**g**) Porphyroblast of scapolite consuming plagioclase, tremolite and calcite. (**h**) Wollastonite invading calcite and quartz. All photomicrographs were taken with transmitted cross-polarized light (XPL). Abbreviations: Cal = calcite, Di = diopside, Ep = epidote, Grs = grossular, Mt = magnetite, Phl = phlogopite, Pl = plagioclase, Qz = quartz, Scp = scapolite, Tr = tremolite, Wo = wollastonite

is also enriched in andradite and almandine components ($Adr_{8-21}Sps+Alm_{6-13}$; ESM Fig. S2c) with no chemical differences between crystal cores and rims. Scapolite occurs as large crystals with a poikiloblastic texture and overgrew after plagioclase (An_{29-30}), calcite, and tremolite, often including diopside, tremolite, and quartz (Fig. 4g). It is classified as meionite (Mei_{57-69}, EqAn between 0.537 and 0.636). Wollastonite occurs as aggregated acicular crystals (Fig. 4h).

Bodó district skarns

The prograde skarn assemblage is composed of diopside, grossular, quartz, plagioclase, titanite, and apatite, while the most common retrograde minerals include epidote, vesuvianite, calcite, quartz, wollastonite, and prehnite (Fig. 5). The composition of skarn minerals is given in ESM Table S8.

The skarns are dominated by second-generation, coarse garnet crystals comprising more than 90% of the rock volume in some portions. Garnet often occurs in straight grain boundary with quartz (Fig. 3f-h), making it challenging to establish an accurate relationship with the preceding mineral assemblages. Garnet-bearing skarns locally exhibit a porous texture (Fig. 3h). This texture is correlated with higher ore grades. The textural relationship between mineral phases indicates a complex evolution for the studied rocks, as the former assemblage was overprinted by the second generation of grossular (II). First-generation grossular (I) is distinguished from grossular II by its smaller grain size and hypidioblastic to idioblastic texture. Grossular I occurs with diopside, plagioclase, and quartz, representing the first minerals formed during the prograde stage (Fig. 5a-b). As in marbles, grossular is the most abundant garnet endmember, while other components occur in minor proportions ($Gr_{70-84}Adr_{5-21}Alm+Sps_{6-13}$; ESM Fig. S2c). The composition of clinopyroxene corresponds to diopside ($Di_{70-92}Hd_{7-28}Jo_{1-4}$; ESM Fig. S2a), and the X_{Mg} values range between 0.716 and 0.929. Centimeter-scale garnet crystals (grossular II) and quartz overprint the previous mineral assemblage (Fig. 5c-e). The mineral assemblage that formed prior to grossular II exhibits corroded borders and textural evidence of disequilibrium caused by interaction with the garnet-forming fluid (Fig. 5c-d).

The retrograde stage comprises recrystallization and deposition of calcite, vesuvianite, epidote/clinozoisite, quartz, wollastonite, and prehnite (Figs. 3i and 5e-h). Vesuvianite occurs as euhedral to subhedral porphyroblastic crystals, often in straight contact or partially including grossular II (Fig. 5e). Vesuvianite commonly contains multiple tiny inclusions of quartz and diopside (Fig. 5e). Epidote/clinozoisite partially replaced diopside, garnet, and vesuvianite (Fig. 5d-f) and filled fractures within these minerals (Fig. 5g). Epidote grains also filled interstitial spaces between garnet crystals and often show diopside inclusions (Fig. 5d). Epidote has X_{Fe} between 0.102 and 0.246. Wollastonite occurs as acicular crystals near the marble contact and often shows quartz inclusions (Fig. 5h). Prehnite filled fractures in garnet and occurs as porphyroblasts encompassing crystals of plagioclase, epidote, garnet, and calcite (Fig. 5h). Quartz is present in all stages of the Bodó skarn formation. Pervasive opal with garnet and scheelite inclusions deposited in the final stage. Late zeolite is commonly associated with opal.

The ore stage is mainly represented by scheelite (I and II) and molybdenite with minor pyrite and chalcopyrite. Scheelite I (Fig. 6a-b) occurs as fine-grained crystals and may be completely or partially enclosed by grossular II, which shows corroded borders. Scheelite I represents the main ore phase. Scheelite II (Fig. 6c-d) features crystals that reach 8 cm in size and is often associated with porous skarn. Scheelite II may be surrounded by opal and exhibits corroded borders. Molybdenite occurs in association with quartz, either in veins or disseminated in the skarn matrix, alongside disseminated pyrite and chalcopyrite.

To summarize, the evolution from marbles to skarns in the Bodó district involved the formation of a primary metamorphic silicate assemblage containing phlogopite, tremolite, and diopside (Fig. 7). Subsequently, metasomatism led to the deposition of wollastonite, grossular (I and II), and scapolite in the marble. The metasomatism involved skarn formation and was characterized by the crystallization of diopside, grossular I, plagioclase, scheelite I, and molybdenite in the prograde stage. The prograde-stage minerals were subsequently overprinted by grossular II. The formation of vesuvianite, epidote, calcite, wollastonite, and prehnite occurred in the retrograde stage, along with the deposition of scheelite II and sulfide minerals.

Geochronology

The Macambira pluton (sample BDD-17) is a medium- to coarse-grained biotite syenogranite. Zircons exhibit euhedral bipyramidal shapes and are 150–300 μm long, with aspect ratios ranging from 2 to 4. They commonly show oscillatory or parallel zoning (Fig. 8a). Some grains exhibit weak compositional variations and enrichment in U in rims compared to cores. Apatite is commonly present as inclusions in these zircons. After excluding the analyses that were discordant or characterized by large errors in their individual analyses, eleven analyses yield a Concordia and weighted mean date of 534.9 ± 3.6 Ma (2σ; Fig. 8b-c).

The $^{40}Ar/^{39}Ar$ dates were obtained on biotite from the Macambira pluton and on muscovite from a pegmatite dike (sample BDD-9) and a mylonite (sample DH10-3). Data are shown in Fig. 9 and summarized in Table 1. The two biotite

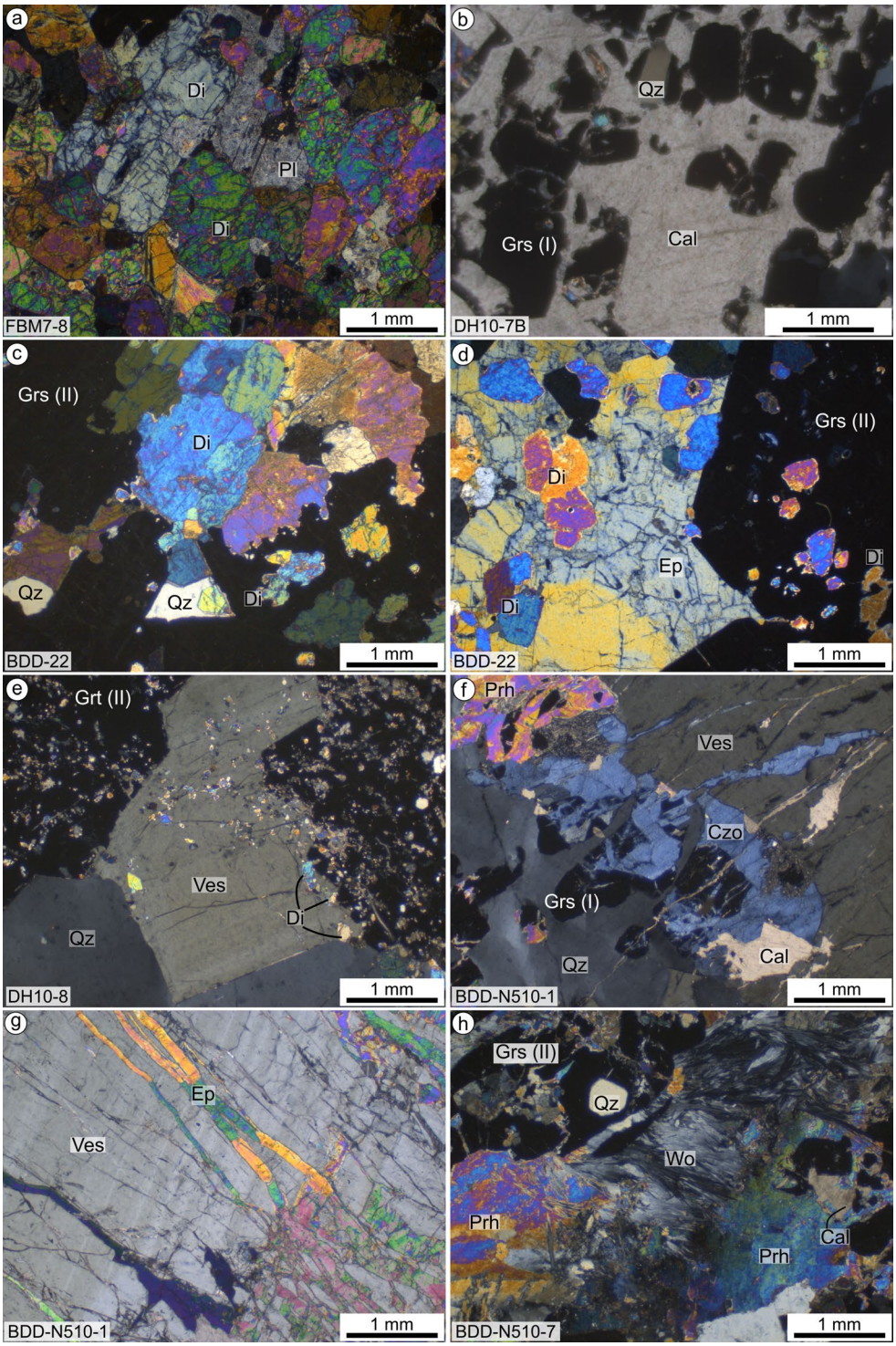

Fig. 5 Photomicrographs of the main skarn mineral assemblages. (**a**) Diopside in contact with plagioclase replaced by white mica. (**b**) Hypidioblastic to idioblastic grossular crystals of the first generation (grossular I) and interstitial quartz with pervasive late calcite. (**c**) Diopside inclusions in a large garnet crystal. All pyroxene borders in contact with garnet are irregular, indicating pyroxene corrosion prior to garnet deposition. (**d**) Large interstitial epidote between coarse-grained garnets, both containing clinopyroxene inclusions. (**e**) Hypidioblastic porphyroblasts of vesuvianite and quartz occur interstitially between large garnet crystals, with a significant amount of fine clinopyroxene inclusions within the former and latter minerals. (**f**) Vesuvianite–quartz assemblage showing garnet inclusions, all exhibiting prehnite and calcite filling microfractures and vugs. (**g**) Veins of epidote crosscutting vesuvianite. (**h**) Grossular II with quartz inclusions and retrograde mineral assemblage composed of prehnite, wollastonite and calcite. All photomicrographs were taken with transmitted, cross-polarized light (XPL). Abbreviations: Cal = calcite, Di = diopside, Ep = epidote, Grs = grossular, Pl = plagioclase, Prh = prehnite, Qz = quartz, Ves = vesuvianite

aliquots provided similar spectra with pronounced $^{40}Ar^*$ loss at lower and intermediate temperatures, representing 30–45% of the total ^{39}Ar released. The sample BDD-17 yielded two distinct 'mini-plateaus' (Fig. 9a) whose weighted mean dates are 491.08 ± 2.35 Ma (0.48% error; 42% ^{39}Ar) and 488.74 ± 2.65 Ma (0.54% error; 25% ^{39}Ar), which overlap at the 2σ level. Together, these data provided a weighted mean date of 490.65 ± 0.67 Ma (Fig. 9b).

The $^{40}Ar/^{39}Ar$ dates on muscovite from pegmatite (BDD-9) and mylonite (DH10-3) samples overlap within analytical error (Fig. 9c). The replicates of the BDD-9 muscovite yielded plateau dates of 501.75 ± 2.36 Ma (0.47% error; 76% ^{39}Ar) and 501.87 ± 2.62 (0.52% error; 86% ^{39}Ar), and provided a

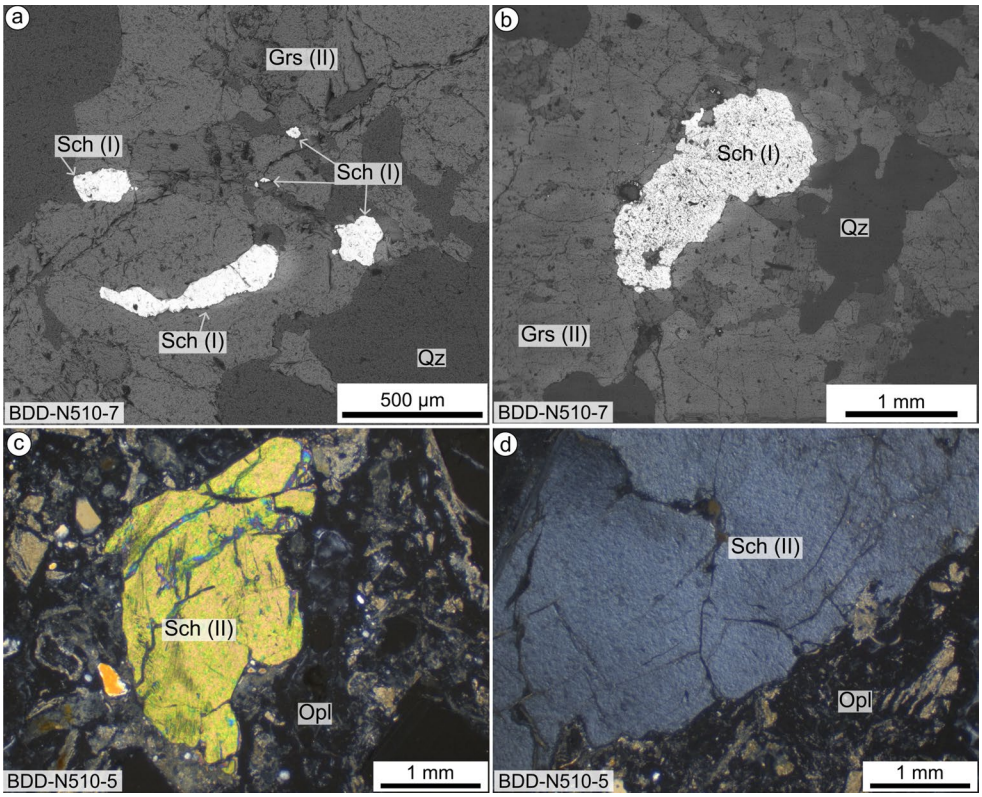

Fig. 6 (**a**) SEM backscattered electron (BSE) image of first generation scheelite (I) included in grossular of the second generation (II). (**b**) SEM BSE image of a scheelite I crystal in irregular contact with grossular II. In (**c**) and (**d**), coarse scheelite II crystals encompassed by a mass of opal. (**c**) and (**d**) Photomicrographs taken under transmitted, cross-polarized light (XPL). Abbreviations: Grs = grossular, Opl = opal, Sch = scheelite

weighted mean date of 501.63 ± 0.59 Ma (Fig. 9d); this date is indistinguishable from the dates of the two DH10-3 aliquots from the mylonite (Fig. 9e), 498.24 ± 2.39 Ma (0.48% error; 86% ^{39}Ar) and 501.41 ± 2.31 Ma (0.46% error; 76% ^{39}Ar). Together, these data yield an integrated weighted mean date of 500.24 ± 0.57 Ma (Fig. 9f). The muscovite from the mylonite is richer in K (K/Ca$_{average}$ ~112) than the muscovite from the pegmatite (K/Ca$_{average}$ ~21).

Carbon and oxygen stable isotopes

The carbon and oxygen isotopic compositions of a total of 44 calcite samples from marbles and skarns were analyzed (ESM Table S6; ESM Fig. S3). Previous data from Nascimento et al. (2004) and Sial et al. (2015) has been compiled. The calcite from regional marbles are characterized by $\delta^{13}C$ values between + 10.08‰ and − 1.17‰ and $\delta^{18}O$ values between + 20.08 and + 27.43‰ (ESM Fig. 3). The isotopic compositions of calcite from skarns and marbles of the Bodó district exhibit a more restricted $\delta^{13}C$ range, from + 7.72 to -7.46‰, but a broader $\delta^{18}O$ range, from + 20.87‰ to of + 9.16‰.

T-XCO$_2$ pseudosections of marble samples

To evaluate the effects of possible contact metamorphism and subsequent metasomatism, two isobaric T–XCO$_2$ pseudosections were calculated at 3 kbar (Fig. 10) using the bulk-rock compositions of marbles with different mineral assemblages. The pressure chosen is compatible with metamorphic (Lima 1992; Souza et al. 2007; Cioffi et al. 2021) and skarn-forming conditions estimated for the Seridó Belt (Souza Neto et al. 2008). Sample BDD-15 consists of calcite, phlogopite, tremolite, diopside, scapolite, and plagioclase, whereas sample BDD-1.6 includes calcite, garnet, diopside, quartz, and plagioclase.

In the pseudosection for sample BDD-15 (Fig. 10a), the mineral assemblage observed in the rock relates to 675 °C at XCO$_2$ = 0.9 to temperatures below 500 °C at XCO$_2$ ≤ 0.1. Above this field, scapolite is absent, and it may represent the first assemblage. Phlogopite occurs under a wide range of temperatures. The compositional isopleths of X_{Mg} in phlogopite and diopside, and of X_{An} in plagioclase indicate a range of peak stabilities at ~650 °C. Although amphibole is present under almost all conditions, the X_{Mg} amphibole isopleths indicate stability only below ~ 575 °C. The scapolite isopleths were not contoured because of the compositional discrepancies between the modeled scapolite and the analyzed mineral.

In sample BDD-1.6 (Fig. 10b), the mineral assemblage is represented by a wide range of stability conditions in the calculated pseudosection. Garnet with the observed composition (indicated by X_{Grs} isopleths) occurs only at low values of XCO$_2$. The combination of diopside and calcite isopleths

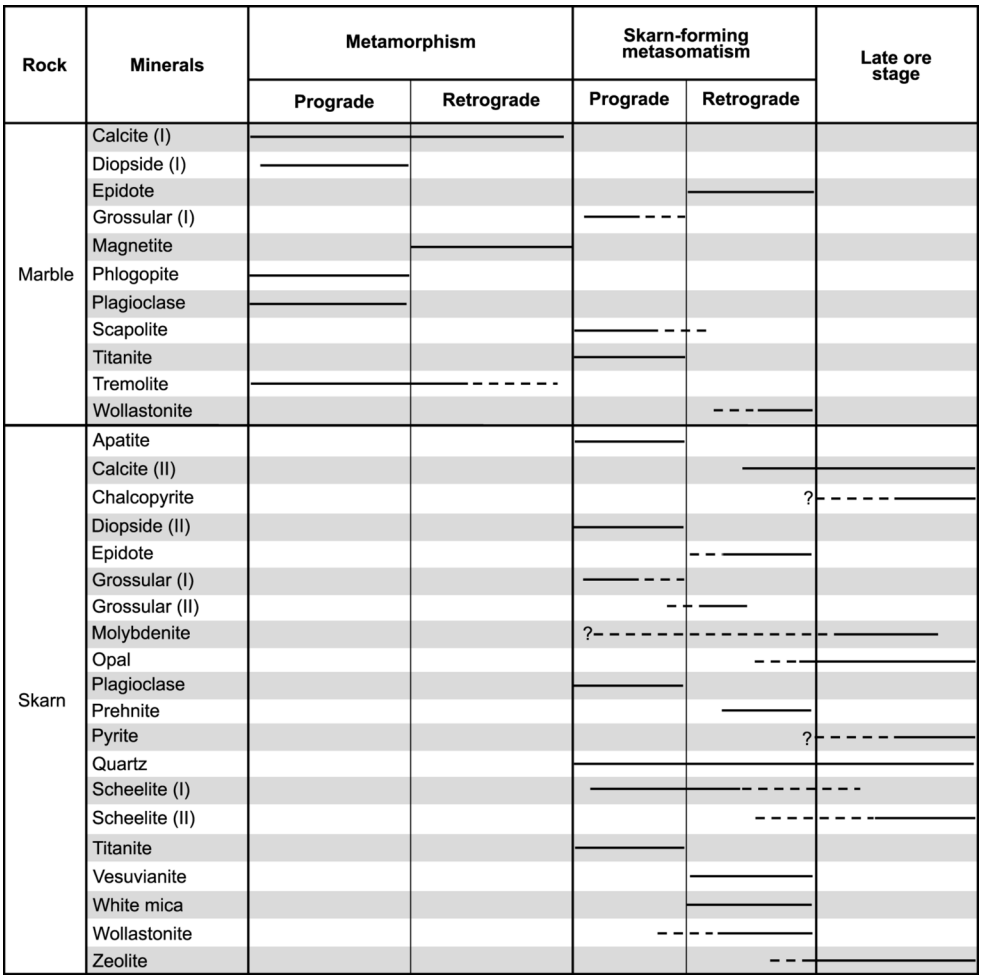

Fig. 7 Paragenetic sequence of marble and skarn in the Bodó district

shows that the clinopyroxene formed at higher temperatures (~600 °C) and at higher XCO_2 than the garnet. Therefore, garnet formation required a decrease in XCO_2 (< 0.2).

Discussion

C–O isotope modeling

The primary control on skarn formation in the Bodó district was lithologic. With minor exceptions, most of the skarns mapped in this area exist within marble lenses interlayered with paragneiss of the Jucurutu Formation or along the marble/paragneiss interface. As argued above, the marble of the Bodó district is variably affected by metasomatic modifications promoted by interactions with magmatic fluids on a regional scale. The original metamorphic mineral assemblage was likely dominated by calcite with phlogopite > tremolite or diopside, with the presence of diopside instead of tremolite being dictated by variations in the temperature conditions. In contrast, the metasomatic minerals are garnet ± wollastonite or scapolite.

Based on a comprehensive geochemical and isotopic (C and Sr) study of the well-preserved marble lenses of the basal Jucurutu Formation and a few preserved examples from the upper Seridó Formation schists, Nascimento et al. (2004, 2007) showed that regional metamorphism was an isochemical process, retaining the original (i.e., sedimentary) isotopic signature of the carbonate protoliths along many of the studied stratigraphic profiles even under amphibolite-facies conditions. They showed that the $\delta^{13}C$ values of the Jucurutu marble lenses vary broadly, from + 11‰ to near 0‰, with similar $\delta^{18}O$ value intervals. These isotopic data, together with the results obtained for the marble lenses in this work and for the skarns in the Bodó district, are plotted in Fig. 11. For clarification, the variation in the $\delta^{13}C$ values of the regional marbles obtained by Nascimento et al. (2004, 2007) was sorted in accordance with a palinspastic restoration of their stratigraphic position within the sedimentary succession: The marble lenses occurring in the lower stratigraphic levels of the Jucurutu Formation were referred to by those authors as the '1st level' group, while the uppermost lenses were referred to as the '3rd level' group. Lenses within the upper Seridó schists

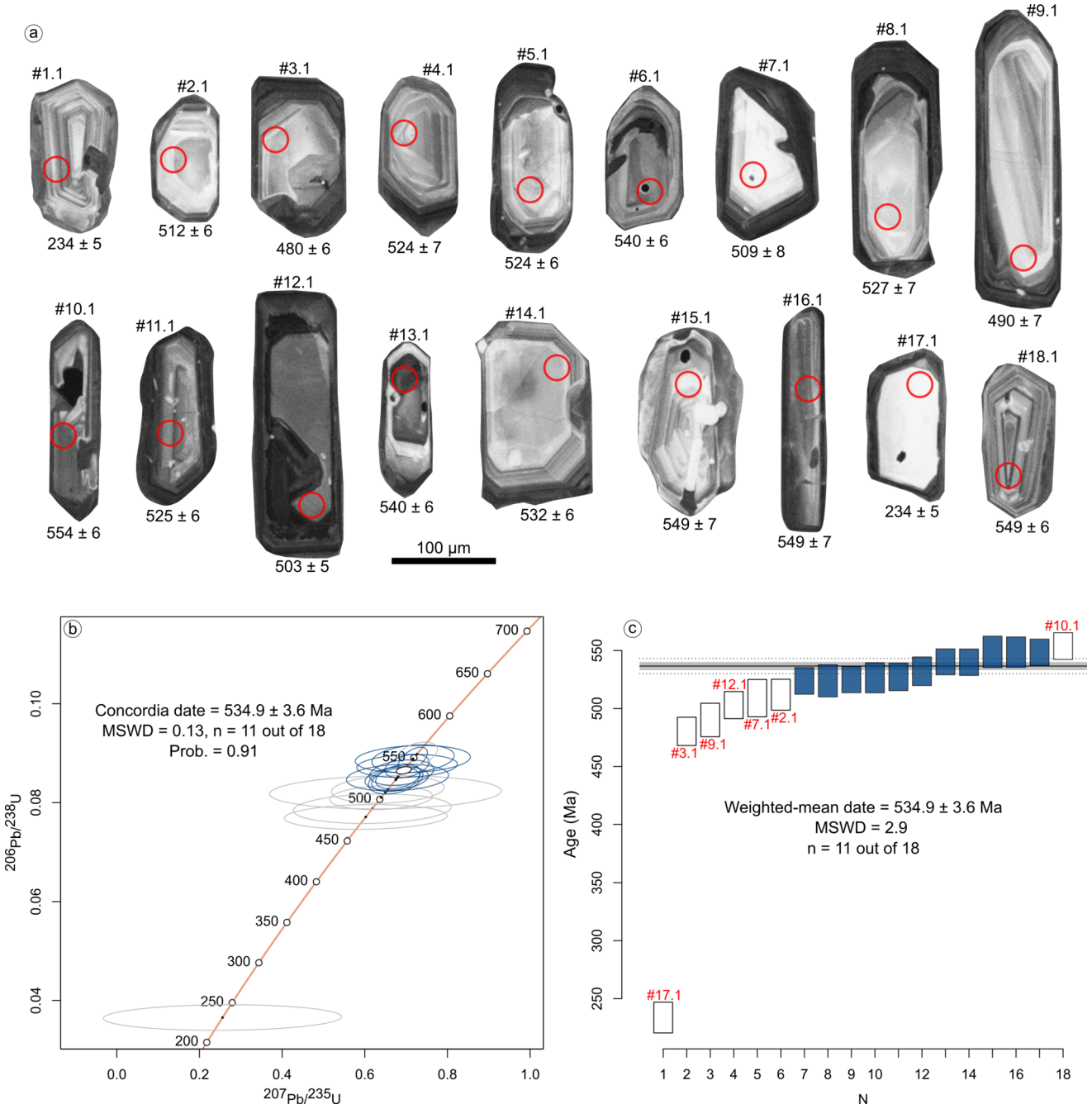

Fig. 8 Cathodoluminescence images of analyzed zircon grains (**a**) and U-Pb zircon dates (**b-c**) of the Macambira granite (sample BDD-17). (**a**) U–Pb concordia diagram and (**b**) $^{206}Pb/^{238}U$ weighted-mean diagram. In (**a**) analyzed spots are indicated with $^{206}Pb/^{238}U$ dates (in Ma) at 1σ errors. In (**b-c**) grey ellipses and unfilled rectangles are the excluded samples from date calculation

were undivided, and their isotopic compositions were not included here. We drew mixing curves with variable CO_2 mole fractions to model the extent of magmatic fluid–carbonate rock interactions, assuming that the initial $\delta^{13}C$-$\delta^{18}O$ rock compositions corresponded to the average values of the primary compositions of the 1st - and 3rd -level groups, magmatic component featured values of $\delta^{13}C$ = -8‰ and $\delta^{18}O$ = + 6‰ according to Bowman (1998), and T = 550 °C. The curves were calculated according to the models of Taylor (1974, 1977) using the isotopic fractionation models proposed by Ohmoto and Ryes (1979) and Zheng (1999) for carbon and oxygen, respectively. The calculations were performed using the Alpha Delta web tool of Beaudoin and Therrien (2009).

Several findings arise from the C–O data in the diagram. First, the carbon and oxygen isotopic compositions

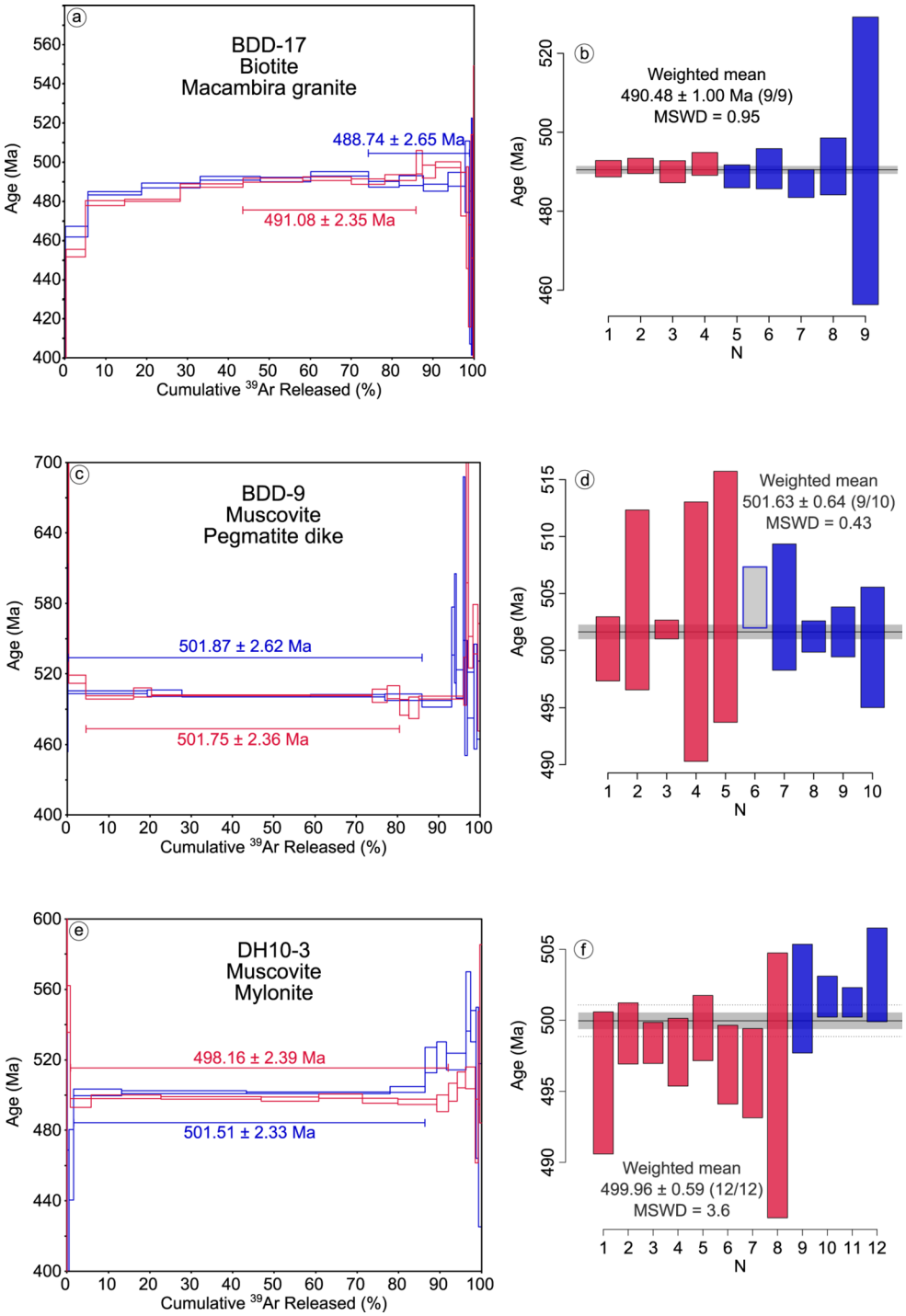

Fig. 9 $^{40}Ar/^{39}Ar$ age spectra of the two aliquots and weighted mean diagrams for the two combined replicates of biotite from the Macambira granite in (**a**) and (**b**); muscovite from a pegmatite dike in (**c**) and (**d**); and muscovite from a mylonite in (**e**) and (**f**). In the weighted mean diagrams, the gray rectangular boxes represent outliers

of most of the studied calcite samples, whether from marble or skarn, plot on mixing lines departing from either the regional 1st - or 3rd -level compositions toward the magmatic endmember.

Most skarn calcite samples exhibit a depletion trend consistent with a fluid–rock interaction model since carbon and oxygen depletion in heavy isotopes cannot be entirely produced by decarbonation/devolatilization processes. All mixing lines were determined using different XCO_2 values, and the effect of decarbonation was modeled for temperatures of 300 and 550 °C (Fig. 11). In this model, all carbon can be released as CO_2, while only 40% of oxygen can be liberated from the rock (calc-silicate limit; Valley 1986). The interaction of externally derived fluids from magmatic sources is common in contact metamorphism and skarn systems (Bowman 1998; Shin and Lee 2003; Timón et al.

Table 1 Summary of $^{40}Ar/^{39}Ar$ geochronology data for the studied samples. Two aliquots were analyzed for each sample

Sample	Rock	Mineral	Date ± 2σ (Ma)	MSWD	Date type	^{39}Ar%	*n*	WM date ± 2σ (Ma)	MSWD
BDD-17 #1	Macambira granite	Biotite	491.08 ± 2.35	1.65	MP	42.32	4(18)	490.48 ± 1.00	0.95
BDD-17 #2			488.74 ± 2.65	2.18		24.72	5(16)		
BDD-9 #1	Pegmatite dike	Muscovite	501.75 ± 2.36	2.1	P	75.98	5(16)	501. 63 ± 0.64	0.43
BDD-9 #2			501.87 ± 2.62	6.13		85.67	5(16)		
DH10-3 #1	Mylonite	Muscovite	498.16 ± 2.39	3.39	P	91.16	8(18)	499.0.96 ± 0.59	3.6
DH10-3 #2			504.51 ± 2.33	1.76		84.75	4(15)		

n: Number of steps used in the age calculation; parentheses indicate the total number of degassing steps. Date type: MP: mini-plateau date, P: plateau date. WM: Weighted mean date for both aliquots

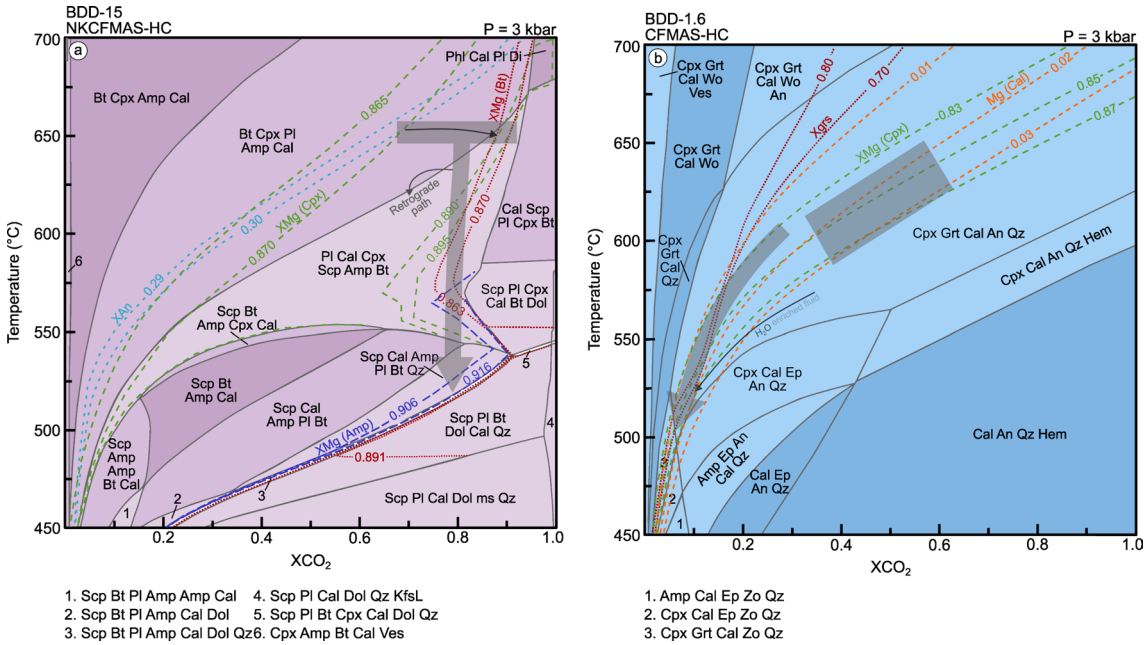

Fig. 10 Pseudosections for samples (**a**) BDD-15 and (**b**) BDD-1.6. (**a**) T-XCO_2 conditions were estimated using intersections of the compositional isopleths of biotite, plagioclase, clinopyroxene and amphibole. The peak mineral assemblage is indicated by the gray polygon. The gray arrow represents a schematic retrograde cooling path. The black arrow indicates the change in CO_2 needed to form scapolite without a temperature change. (**b**) Intersections of compositional isopleths of garnet, clinopyroxene and calcite indicate that the field best represents the high-temperature stage (gray polygon). The gray arrow represents a schematic path derived from an increase in H_2O. Amp = amphibole, An = anorthite, Bt = biotite, Cal = calcite, Cpx = clinopyroxene, Dol = dolomite, Ep = epidote, Grt = garnet, Hem = hematite, Kfs = k-feldspar, Phl = phlogopite, Pl = plagioclase, Qz = quartz, Scp = scapolite, Ves = vesuvianite, Wo = wollastonite, Zo = zoisite

2007; Orhan et al. 2011). The data in Fig. 11 reveal that different stratigraphic levels of the regional marbles in the Jucurutu Formation are needed to fit the modeled mixing lines between sedimentary and magmatic endmembers. This interpretation is supported by the two distinct groups of mixing lines along which almost all the samples plot, indicating the need for different sedimentary signatures. Moreover, calcite from all deposits shows a trend toward the igneous field, suggesting interactions with magmatic fluids.

Two samples of late calcite formed during the retrograde stages of the Bodó District skarns also plot within the magmatic field, indicating a pure igneous signature (Fig. 11). The data dispersion across the multiple curves may suggest that marble, skarn, and late calcite interacted with fluids over a wide range of XCO_2 values, varying from 0.5 to almost 0.01, and at different fluid: rock ratios, which is plausible since skarn systems are widely heterogeneous (Meinert et al. 2005; Gaspar et al. 2008; Ismail et al. 2014). This interaction was probably not coeval throughout all the marble and skarn lenses and could have happened under different temperature conditions over time. A higher temperature than the one used in the modeling would shift the mixing lines to the left, whereas a lower temperature would lead to a shift to the right. Nonetheless, the fluid–rock interaction model was calculated using only a temperature of 550 °C for simplification purposes, which is a reasonable estimation of the prograde–retrograde transition. Samples that plot below the mixing lines must result from an exchange between magmatic fluid and $\delta^{13}C$-depleted graphite or from the interaction with CH_4-rich fluids, indicating the presence

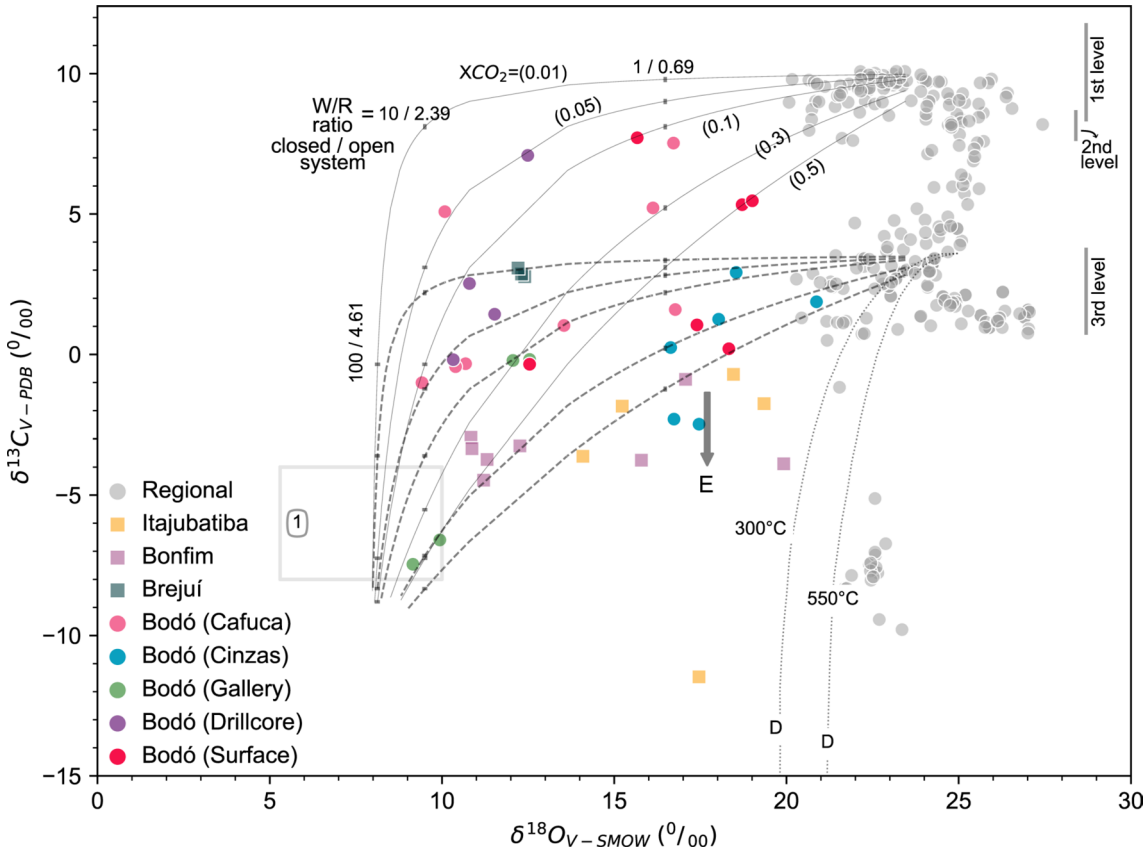

Fig. 11 $\delta^{18}O$ versus $\delta^{13}C$ diagram for samples from the Bodó District compared to other major deposits from the Seridó Belt and the regional marble of the Jucurutu Formation. The three Jucurutu levels are highlighted in the graph according to the interpretation by Nascimento et al. (2004). The gray curves represent mixing lines for fluid/rock interactions at 550 °C from initial values of 10‰ and 25‰ for $\delta^{13}C$ and $\delta^{18}O$, respectively, whereas the dashed gray lines represent initial values of 3.5‰ and 25‰ for $\delta^{13}C$ and $\delta^{18}O$, respectively. Ticks indicate fluid: rock ratios for closed and open systems, with values of 1/0.69, 10/2.39 and 100/4.61, respectively, following the same sequence on all curves. Field 1 represents primary magmatic waters from Sahlström et al. (2019) after Taylor (1974, 1986, 1992), Sheppard (1981), Valley (1986), and Bowman (1998). The D dotted lines indicate decarbonation paths. Arrow E indicates the qualitative effect of exchange with $\delta^{13}C$-depleted graphite or CH_4-rich fluids

of organic matter. All the alternatives above could result in a trend following arrow E in Fig. 11.

Linking magmatic events to skarn formation in the Bodó district

Tungsten skarns are commonly associated with differentiated calc-alkaline metaluminous to peraluminous granites of crustal origin (Meinert et al. 2005; Hulsbosch et al. 2016; Legros et al. 2020). Skarn formation in the Seridó Mineral Province has been classically linked to the regional-scale intrusion of high-K calc-alkaline granitic plutons that are usually spatially associated with the main deposits (Souza Neto et al. 2008; Santos et al. 2014). One of the best studied districts of the Seridó Mineral Province, Brejuí-Boca de Lage district, which includes the Brejuí deposit and nearby occurrences (Cavalcante et al. 2016), had been inferred to be associated with the intrusion of the Acari batholith. However, zircons from the porphyritic and equigranular granitic facies that constitute the bulk of the batholith were dated at ca. 577 Ma and 572 Ma, respectively (Archanjo et al. 2013), in clear dissociation with the Re-Os molybdenite date at ca. 554 Ma obtained by Hollanda et al. (2017).

The Re–Os system in molybdenite is a robust geochronometer for mineralization because it is a resilient system during high-grade metamorphism and deformation (Stein et al. 2001) with a relatively moderate to high closure temperature (~500 °C; Suzuki et al. 1996). Thus, Re–Os dates are widely used to determine the crystallization age of molybdenite during hydrothermal stages (Stein et al. 2001; McInnes 2005; Chiaradia et al. 2013) and are integrated with U–Pb and $^{40}Ar/^{39}Ar$ dates on igneous bodies to link magmatism and hydrothermal mineralization (Li et al. 2020, 2021; Zhang et al. 2020).

Magmatic activity throughout the Bodó district started at ca. 534 Ma while the thermal activity in the district ended at ca. 490 Ma (Fig. 12). The W–Mo mineralization occurred at 510 ± 2 Ma, as constrained by Re–Os dating of

molybdenite (Hollanda et al. 2017). Considering the closure temperature of the Re-Os system and the temperature for the Bodó district skarns obtained in this work, the Re-Os date can be attributed to the transition from the prograde stage to the retrograde stage. This date is significantly younger than the ca. 534 Ma date of the nearest granite, the high-K calc-alkaline magmatic Macambira pluton. This indicates that the magmatic fluids related to the mineralization were not derived from this granite body. In contrast, the Re-Os molybdenite date matches a set of U–Pb ID TIMS dates in the range between 515 and 509 Ma on columbite-tantalite from homogeneous and heterogeneous pegmatites exposed within the Seridó Mineral Province (Baumgartner et al. 2006). Since the U–Pb systematics in columbite-tantalite are comparable to the U–Pb systematics in zircon in a way that both represent crystallization ages (e.g., Romer and Wright 1992; Romer and Smeds 1994), the dates obtained by Baumgartner et al. (2006) are the best estimates for the crystallization age of the pegmatitic magmas in the Seridó Mineral Province. Therefore, considering the available data so far, these dates are used here to establish a connection between the source of magmatic-hydrothermal ore fluids with pegmatites. The source of heat and fluid for skarn formation, however, requires further investigation. In this sense, some possibilities involve skarn formation during regional metamorphism (Lefebvre et al. 2019a, b; Romer et al. 2022) or during Ediacaran granitic magmatism, followed by later metal enrichment and/or remobilization as a result of granitic pegmatite emplacement.

The $^{40}Ar/^{39}Ar$ plateau date of 501.9 ± 2.7 Ma obtained for a local E–W-trending pegmatite dike reflects the cooling age of this volatile-rich magma. The coincidence of the $^{40}Ar/^{39}Ar$ dates in muscovite and biotite from pegmatite, granite, and mylonite rocks at 500 – 490 Ma corresponds to the cooling stage of the Seridó Belt (Corsini et al. 1998) with temperatures between 310 and 280 °C (assuming experimental cooling rates ranging from 10 to 1 °C/Ma; Harrison et al. 1985), and the late reactivation of shear zones on a regional-to-local scale.

Metamorphic/metasomatic evolution

Phase equilibria modeling of skarns is challenging due to their chemical, textural, and mineralogical heterogeneity. This has led to an extrapolation of the interpretations obtained from the marbles, as both skarn and marble share a common mineralogy. The results obtained through pseudosection modeling show that the peak temperature ranged between 650 and 600 °C at different XCO_2 depending on the main mineral assemblage (Fig. 10). These temperature estimates agree with the geothermometry calculations obtained by Sallet et al. (2021) for the Seridó schists and Jucurutu gneiss at the contact with the pegmatites. In sample BDD-15, petrographic observations indicate that scapolite formed after the main silicate phases represented by the field composed of diopside–phlogopite–tremolite–plagioclase–calcite. The scapolite growth encompassing the other mineral phases suggests a fluid-induced process and provides evidence of a Cl-rich fluid, as shown by electron probe micro-analysis (Cl ranging from 0.109 to 0.237 a.p.f.u.). Scapolite-bearing rocks usually form in the presence of CO_2-rich fluids (Aitken 1983; Kwon et al. 2020),

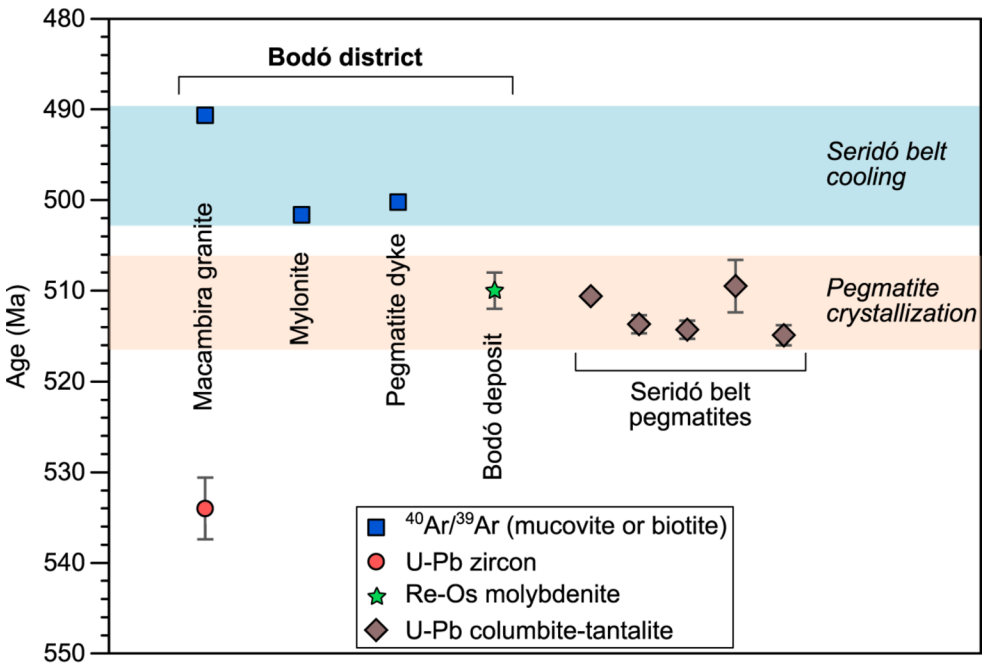

Fig. 12 Summary of Cambrian geochronological data from the Bodó district and U–Pb ages of columbite-tantalite from other pegmatites in the Seridó Mineral Province (data from Baumgartner et al. 2006). Re–Os molybdenite age from Hollanda et al. (2017)

supporting the results of the presented pseudosection, in which an increase in XCO_2 marks the transition towards the scapolite field under near-isothermal conditions (black arrow in Fig. 10). The incursion of acicular crystals of wollastonite in the marble suggests a process induced by fluids commonly associated with Si-rich metasomatism (Fig. 4h). The retrograde path, marked in the pseudosection by the compositions of amphibole and phlogopite, indicates a temperature decrease to below ~ 575 °C.

The mineral assemblage of sample BDD-1.6 shows slightly different XCO_2 conditions for the formation of garnet. Although clinopyroxene is stable under a wide range of T-XCO_2 conditions, compositional garnet isopleths are limited to a narrow field at lower XCO_2. The proposed evolution path started at ~ 600 °C and was characterized by the crystallization of the diopside–phlogopite–plagioclase–calcite association. Grossular II could only have formed in response to a decrease in XCO_2 induced by H_2O influx in the system. The assemblage composed of clinopyroxene–grossular I–calcite–plagioclase–quartz can be stable over a wide range of XCO_2 values, whereas the late grossular II assemblage is stable only under low XCO_2 (< 0.2) conditions.

Including the skarns in these interpretations, fluid-induced processes (e.g., metasomatism) evidently played an important role in the genesis of the studied rocks. An open system setting is supported by the presence of monomineralic garnet zones (Korzhinskii 1965; Putnis and Austrheim 2010), cm-sized garnet porphyroblasts (Fig. 5c-e), and vesuvianite, wollastonite, garnet, and scapolite with textural evidence of growth along corroded borders.

The decrease in XCO_2 in the fluid (from 0.6 to > 0.1) led to the replacement of early pyroxene by garnet in the marble and skarn (Fig. 10). This large variation in XCO_2 could be explained by the heterogeneities observed in skarn systems and is consistent with the data obtained from carbon and oxygen stable isotopes, which indicate that XCO_2 can range from approximately 0.01 to above 0.5 (Fig. 11).

Conclusions

The data obtained in this study lead to the following conclusions

- C and O stable isotope signatures of calcite from the Jucurutu marble lenses did not change during regional metamorphism. In contrast, depletion in isotopically heavy C and O occurred during metasomatic events triggered by the circulation of hydrothermal fluids of magmatic origin. Consequently, mixing lines between the regional Jucurutu marble and a magmatic endmember are consistent with a fluid–rock interaction model in which the observed carbon and oxygen isotope depletions could not have been produced by devolatilization alone.
- Wide variation in C and O isotope values, and corresponding range in fluid XCO_2 at different fluid: rock ratios, indicates a system with significant variability in its fluid composition during the formation of the different mineral assemblages.
- T-XCO_2 pseudosections produced for marbles indicate a peak metamorphic temperature of 650–600 °C at different XCO_2 values depending on the main mineral assemblage. The formation of coarse garnet required a decrease in XCO_2 and, consequently, a higher H_2O influx than required for clinopyroxene formation. In contrast, scapolite in the Bodó district marbles would have formed at almost isothermal conditions at ~ 650 °C with an increase in XCO_2. The transition from prograde to retrograde stage started at ~ 550–500 °C as indicated by the crystallization of the second generation of garnet (i.e., garnet II) and tremolite.
- The integration of new U–Pb zircon (536.6 ± 3.4 Ma) and $^{40}Ar/^{39}Ar$ biotite (490.48 ± 1.00 Ma) dates for the Macambira granite, as well as a $^{40}Ar/^{39}Ar$ muscovite date for a local pegmatitic dike (501.36 ± 0.59 Ma), coupled with a previously reported Re–Os molybdenite date (510 ± 2 Ma) for the Bodó deposit, and U–Pb zircon dates for the Seridó Mineral Province pegmatites (515–509 Ma) reveal that skarn mineralization was likely coeval with the emplacement of the pegmatitic dikes and stocks, while the $^{40}Ar/^{39}Ar$ dates represent cooling ages for the regional magmatic-hydrothermal system.
- The data presented in this study contribute to unraveling the complex metamorphic, metasomatic, and magmatic processes related to W-skarn mineralization in the Seridó Mineral Province. The results shed light on the skarn and marble formation conditions, the role of fluid-rock interactions, and ore-forming fluid sources. The integration of novel and published data provides insights for further investigation of the magmatic-hydrothermal system, and the potential for metal exploration in the Seridó Mineral Province.

Supplementary Information The online version contains supplementary material available at https://doi.org/10.1007/s00126-024-01300-4.

Acknowledgements D. Lucas thanks the Brazilian Federal Agency for Support and Evaluation of Graduate Education (CAPES) for the MSc scholarship (grant 88887.597991/2021-00). M. H. B. M. Hollanda, J. A. Souza Neto, and R. Moraes thank National Council for Scientific and Technological Development (CNPq) for the research fellowships (grants 311.146/2022-8, 313.251/2021–5, and 304.696/2023-4). D. Lucas and M. H. B. M. Hollanda thank São Paulo Support Foundation (FUSP) for financial support (grant 318720). We would like to express

our gratitude to Associate Editor Lisard Torró for his helpful comments and suggestions, which have significantly enhanced the quality of this paper. Furthermore, we deeply appreciate the constructive feedback from Sava Markovic and an anonymous reviewer. We are also thankful to Maurício França and Bodó Mineração for granting us access to the mine galleries and drill cores, and to Francisco Chagas for guiding us in the mine and sharing his knowledge of the Bodó deposit. Additionally, we extend our thanks to João Victor Pereira and Larisse Cruz for their assistance during the fieldwork. This article is part of D. Lucas MSc thesis conducted at the Universidade de São Paulo.

Author contributions **Dinarte Lucas**: conceptualization, methodology, formal analysis, writing – original draft. **Maria Helena B. M. Hollanda**: conceptualization, methodology, validation, formal analysis, fund acquisition, writing – review & editing. **João A. Souza Neto**: conceptualization, validation, investigation, formal analysis, writing – review & editing. **Renato Moraes**: validation, investigation, methodology, formal analysis, writing – review & editing. **Laécio C. Souza**: writing – review & editing, validation, investigation.

Declarations

Conflict of interest The authors declare no competing interests.

References

Aitken BG (1983) T-XCO_2 stability relations and phase equilibria of a calcic carbonate scapolite. Geochim Cosmochim Acta 47:351–362. https://doi.org/10.1016/0016-7037(83)90258-2

Almeida FFM, Hasui Y, Brito Neves BB, Fuck RA (1981) Brazilian structural provinces: an introduction. Earth-Sci Rev 17:1–29. https://doi.org/10.1016/0012-8252(81)90003-9

Anovitz LM, Essene EJ (1987) Phase Equilibria in the System $CaCO_3$-$MgCO_3$-$FeCO_3$. J Petrol 28:389–415. https://doi.org/10.1093/petrology/28.2.389

Araújo MNC, Alves da Silva FC, Jardim de Sá EF, Holcombe RJ (2002) Geometry and structural control of gold vein mineralizations in the Seridó Belt, northeastern Brazil. J South Am Earth Sci 15:337–348. https://doi.org/10.1016/S0895-9811(02)00040-8

Araújo MNC, Vasconcelos PM, Alves da Silva FC, Jardim de Sá EF, Sá JM (2005) $^{40}Ar/^{39}Ar$ geochronology of gold mineralization in Brasiliano strike-slip shear zones in the Borborema Province, NE Brazil. J South Am Earth Sci 19:445–460. https://doi.org/10.1016/j.jsames.2005.06.009

Araújo Neto JFD, Santos LCMDL, Viegas G, de Souza CP, Miggins D, Cawood PA (2023) Structural and geochronological constraints on the Portalegre shear zone: implications for emerald mineralization in the Borborema Province, Brazil. J Struct Geol 174:104921. https://doi.org/10.1016/j.jsg.2023.104921

Archanjo CJ, Viegas LGF, Hollanda MHBM, Souza LC, Liu D (2013) Timing of the HT/LP transpression in the Neoproterozoic Seridó Belt (Borborema Province, Brazil): constraints from U–Pb (SHRIMP) geochronology and implications for the connections between NE Brazil and West Africa. Gondwana Res 23:701–714. https://doi.org/10.1016/j.gr.2012.05.005

Archanjo CJ, Hollanda MHBM, Viegas LGF (2021) Late ediacaran lateral-escape tectonics as recorded by the Patos shear zone (Borborema Province, NE Brazil). Braz J Geol 51:e20200132. https://doi.org/10.1590/2317-4889202120200132

Baumgartner R, Romer RL, Moritz R, Sallet R, Chiaradia M (2006) Columbite-tantalite-bearing granitic pegmatites from the Seridó Belt, northeastern Brazil: genetic constraints from U–Pb dating and pb isotopes. Can Mineral 44:69–86. https://doi.org/10.2113/gscanmin.44.1.69

Beaudoin G, Therrien P (2009) The web stable isotope fractionation calculator. Handbook of stable isotope analytical techniques. Elsevier, pp 1045–1047

Beurlen H, Da Silva MRR, Thomas R, Soares DR, Olivier P (2008) Nb–Ta–(Ti–Sn) oxide mineral chemistry as tracer of rare-element granitic pegmatite fractionation in the Borborema Province, Northeastern Brazil. Min Deposita 43:207–228. https://doi.org/10.1007/s00126-007-0152-4

Beurlen H, Thomas R, da Silva MRR, Muller A, Rhede D, Soares DR (2014) Perspectives for Li- and Ta-mineralization in the Borborema Pegmatite Province, NE-Brazil: a review. J South Am Earth Sci 56:110–127. https://doi.org/10.1016/j.jsames.2014.08.007

Beurlen H, Rhede D, Thomas R, da Silva M, Soares D (2019) Evaluation of the potential for rare earth element (REE) deposits related to the Borborema Pegmatite Province in northeastern Brazil. Estud Geol 29:40–53. https://doi.org/10.18190/1980-8208/estudosgeologicos.v29n2p40-53

Black LP, Kamo SL, Allen CM, Aleinikoff JN, Davis DW, Korsch RJ, Foudoulis C (2003) TEMORA 1: a new zircon standard for phanerozoic U–Pb geochronology. Chem Geol 200:155–170. https://doi.org/10.1016/S0009-2541(03)00165-7

Black LP, Kamo SL, Allen CM, Davis DW, Aleinikoff JN, Valley JW, Mundil R, Campbell IH, Korsch RJ, Williams IS, Foudoulis C (2004) Improved $^{206}Pb/^{238}U$ microprobe geochronology by the monitoring of a trace-element-related matrix effect; SHRIMP, ID–TIMS, ELA–ICP–MS and oxygen isotope documentation for a series of zircon standards. Chem Geol 205:115–140. https://doi.org/10.1016/j.chemgeo.2004.01.003

Bowman JR (1998) Stable isotope systematics of skarns. In: Lentz DR (ed) Mineralized intrusion-related skarn systems. Mineralogical Association of Canada, Quebec City, Quebec, pp 99–146

Caby R, Arthaud MH, Archanjo CJ (1995) Lithostratigraphy and petrostructural characterization of supracrustal units in the Brasiliano belt of Northeast Brazil: geodynamic implications. J South Am Earth Sci 8:235–246. https://doi.org/10.1016/0895-9811(95)00011-4

Cavalcante R, Cunha ALC da, de Oliveira RG, Medeiros VC, Dantas AR, Costa AP, Lins CAC, Larizzatti JH (2016) Metalogenia das Províncias Minerais do Brasil: Área Seridó-Leste, extremo nordeste da Província Borborema (RN-PB). SGB/CPRM, Brasília

Caxito FA, Santos LCML, Ganade CE, Bendaoud A, Fettous E-H, Bouyo MH (2020) Toward an integrated model of geological evolution for NE Brazil-NW Africa: the Borborema Province and its connections to the trans-saharan (benino-Nigerian and tuareg shields) and Central African orogens. Braz J Geol 50:e20190122. https://doi.org/10.1590/2317-4889202020190122

Caxito FA, Basto CF, Santos LCMDL, Dantas EL, Medeiros VCD, Dias TG, Barrote V, Hagemann S, Alkmim AR, Lana C (2021) Neoproterozoic magmatic arc volcanism in the Borborema Province, NE Brazil: possible flare-ups and lulls and implications for western Gondwana assembly. Gondwana Res 92:1–25. https://doi.org/10.1016/j.gr.2020.11.015

Chiaradia M, Schaltegger U, Spikings R, Wotzlaw J-F, Ovtcharova M (2013) How accurately can we date the duration of magmatic-hydrothermal events in porphyry systems?–An invited paper. Econ Geol 108:565–584. https://doi.org/10.2113/econgeo.108.4.565

Cioffi CR, Meira VT, Trindade RIF, Lanari P, Ganade CE, Gerdes A (2021) Long-lived intracontinental deformation associated with high geothermal gradients in the Seridó Belt (Borborema Province, Brazil). Precambrian Res 358:106141. https://doi.org/10.1016/j.precamres.2021.106141

Connolly JAD (1990) Multivariable phase diagrams; an algorithm based on generalized thermodynamics. Am J Sci 290:666–718. https://doi.org/10.2475/ajs.290.6.666

Connolly JAD (2009) The geodynamic equation of state: what and how. Geochem Geophys Geosyst 10:19. https://doi.org/10.1029/2009GC002540

Coplen TB, Kendall C, Hopple J (1983) Comparison of stable isotope reference samples. Nature 302:236–238. https://doi.org/10.1038/302236a0

Corsini M, Vauchez A, Archanjo C, Jardim de Sá EF (1991) Strain transfer at continental scale from a transcurrent shear zone to a transpressional Fold belt: the Patos-Seridó system, northeastern Brazil. Geology 19:586–589. https://doi.org/10.1130/0091-7613(1991)019%3C0586:STACSF%3E2.3.CO;2

Corsini M, Figueiredo LL, Caby R, Féraud G, Ruffet G, Vauchez A (1998) Thermal history of the Pan-African/Brasiliano Borborema Province of northeast Brazil deduced from $^{40}Ar/^{39}Ar$ analysis. Tectonophysics 285:103–117. https://doi.org/10.1016/S0040-1951(97)00192-3

Dantas EL, Van Schmus WR, Hackspacher PC, Fetter AH, Brito Neves BB, Cordani U, Nutman AP, Williams IS (2004) The 3.4–3.5 Ga São José do Campestre Massif, NE Brazil: remnants of the oldest crust in South America. Precambrian Res 130:113–137. https://doi.org/10.1016/j.precamres.2003.11.002

Dantas EL, Souza ZS, Wernick E, Hackspacher PC, Martin H, Xiaodong D, Li J-W (2013) Crustal growth in the 3.4–2.7 Ga São José De Campestre Massif, Borborema Province, NE Brazil. Precambrian Res 227:120–156. https://doi.org/10.1016/j.precamres.2012.08.006

de Brito Neves BB, Santos EJ, Van Schmus WR (2000) Tectonic history of the Borborema Province, northeastern Brazil. In: Cordani, UG, Milani, EJ, Thomaz Filho, A, Campos, DA (eds) Tectonic evolution of South America. 31st International Geological Congress, Rio de Janeiro, pp 151–182

Diener JFA, Powell R, White RW, Holland TJB (2007) A new thermodynamic model for clino- and orthoamphiboles in the system Na_2O–CaO–FeO–MgO–Al_2O_3–SiO_2–H_2O–O. J Metamorph Geol 25:631–656. https://doi.org/10.1111/j.1525-1314.2007.00720.x

Einaudi MT, Meinert LD, Newberry RJ (1981) Skarn deposits. In: Skinner BJ (ed) Seventy-fifth anniversary volume. Society of Economic Geologists, pp 317–391

Ferreira ACD, Dantas EL, Santos TJS, Fuck RA, Tedeschi M (2020) High-pressure metamorphic rocks in the Borborema Province, Northeast Brazil: reworking of Archean oceanic crust during proterozoic orogenies. Geosci Front 11:2221–2242. https://doi.org/10.1016/j.gsf.2020.03.004

Fossen H, Harris LB, Cavalcante C, Archanjo CJ, Ávila CF (2022) The Patos-Pernambuco shear system of NE Brazil: partitioned intracontinental transcurrent deformation revealed by enhanced aeromagnetic data. J Struct Geol 158:104573. https://doi.org/10.1016/j.jsg.2022.104573

Ganade de Araujo CE, Rubatto D, Hermann J, Cordani UG, Caby R, Basei MAS (2014) Ediacaran 2,500-km-long synchronous deep continental subduction in the West Gondwana Orogen. Nat Commun 5:5198. https://doi.org/10.1038/ncomms6198

Gaspar M, Knaack C, Meinert LD, Moretti R (2008) REE in skarn systems: a LA-ICP-MS study of garnets from the Crown Jewel gold deposit. Geochim Cosmochim Acta 72:185–205. https://doi.org/10.1016/j.gca.2007.09.033

Harrison TM, Duncan I, McDougall I (1985) Diffusion of ^{40}Ar in biotite: temperature, pressure and compositional effects. Geochim Cosmochim Acta 49:2461–2468. https://doi.org/10.1016/0016-7037(85)90246-7

Holland TJB, Powell R (1998) An internally consistent thermodynamic data set for phases of petrological interest. J Metamorph Geol 16:309–343. https://doi.org/10.1111/j.1525-1314.1998.00140.x

Hollanda MHBM, Archanjo CJ, Souza LC, Dunyi L, Armstrong R (2011) Long-lived paleoproterozoic granitic magmatism in the Seridó-Jaguaribe domain, Borborema Province–NE Brazil. J South Am Earth Sci 32:287–300. https://doi.org/10.1016/j.jsames.2011.02.008

Hollanda MHBM, Archanjo CJ, Bautista JR, Souza LC (2015) Detrital zircon ages and nd isotope compositions of the Seridó and Lavras Da Mangabeira basins (Borborema Province, NE Brazil): evidence for exhumation and recycling associated with a major shift in sedimentary provenance. Precambrian Res 258:186–207. https://doi.org/10.1016/j.precamres.2014.12.009

Hollanda MHBM, Souza Neto JA, Archanjo CJ, Stein H, Maia ACS (2017) Age of the granitic magmatism and the W-Mo mineralization in skarns of the Seridó Belt (NE Brazil) based on zircon U-Pb (SHRIMP) and molybdenite re-os dating. J South Am Earth Sci 79:1–11. https://doi.org/10.1016/j.jsames.2017.07.011

Hulsbosch N, Boiron M-C, Dewaele S, Muchez P (2016) Fluid fractionation of tungsten during granite–pegmatite differentiation and the metal source of peribatholitic W quartz veins: evidence from the Karagwe-Ankole Belt (Rwanda). Geochim Cosmochim Acta 175:299–318. https://doi.org/10.1016/j.gca.2015.11.020

Ismail R, Ciobanu CL, Cook NJ, Teale GS, Giles D, Mumm AS, Wade B (2014) Rare earths and other trace elements in minerals from skarn assemblages, Hillside iron oxide–copper–gold deposit, Yorke Peninsula, South Australia. Lithos 184–187:456–477. https://doi.org/10.1016/j.lithos.2013.07.023

Jardim de Sá EF (1994) A Faixa Seridó (Província Borborema, NE do Brasil) e o seu significado geodinâmico na cadeia Brasileira/Pan-Africana. Tese de Doutorado, Universidade de Brasília

Jardim de Sá EF, Fuck RA, Macedo MHDF, Peucat JJ, Kawashita K, Souza ZS, Bertrand JM (1995) Pre-brasiliano orogenic evolution in the Seridó Belt, NE Brazil: conflicting geochronological and structural data. Rev Bras Geociências 25:307–314. https://doi.org/10.25249/0375-7536.1995307314

Koppers AAP (2002) ArArCALC—software for $^{40}Ar/^{39}Ar$ age calculations. Comput Geosci 28:605–619. https://doi.org/10.1016/S0098-3004(01)00095-4

Korzhinskii DS (1965) The theory of systems with perfectly mobile components and processes of mineral formation. Am J Sci 263:193–205. https://doi.org/10.2475/ajs.263.3.193

Korzhinskii DS (1968) The theory of metasomatic zoning. Min Deposita 3:222–231. https://doi.org/10.1007/BF00207435

Kuhn BK (2005) Scapolite stability: Phase relations and chemistry of impure metacarbonate rocks in the Central Alps. PhD thesis, ETH Zurich

Kwak TA (1987) W-Sn skarn deposits and related metamorphic skarns and granitoids. Elsevier, Amsterdam

Kwon S, Samuel VO, Song Y, Kim SW, Park S-I, Jang Y, Santosh M (2020) Eclogite resembling metamorphic disequilibrium assemblage formed through fluid-induced metasomatic reactions. Sci Rep 10:19869. https://doi.org/10.1038/s41598-020-76999-y

Lefebvre MG, Romer RL, Glodny J, Kroner U, Roscher M (2019a) The Hämmerlein skarn-hosted polymetallic deposit and the Eibenstock granite associated greisen, western Erzgebirge, Germany: two phases of mineralization—two Sn sources. Min Deposita 54:193–216. https://doi.org/10.1007/s00126-018-0830-4

Lefebvre MG, Romer RL, Glodny J, Roscher M (2019b) Skarn formation and tin enrichment during regional metamorphism: the Hämmerlein polymetallic skarn deposit. Lithos 348–349:105171. https://doi.org/10.1016/j.lithos.2019.105171

Legros H, Lecumberri-Sanchez P, Elongo V, Laurent O, Falck H, Adlakha E, Chelle-Michou C (2020) Fluid evolution of the Cantung tungsten skarn, Northwest territories, Canada: differentiation

and fluid-rock interaction. Ore Geol Rev 127:103866. https://doi.org/10.1016/j.oregeorev.2020.103866

Li N, Yang F, Zhang Z, Li C (2020) Dating the Xiaobaishitou Skarn W–(Mo) deposit, Eastern Tianshan, NW China: constraints from zircon U–Pb, muscovite ^{40}Ar–^{39}Ar, and molybdenite Re–Os system. Ore Geol Rev 124:103637. https://doi.org/10.1016/j.oregeorev.2020.103637

Li Y, Yuan F, Jowitt SM, Wang F, Li X, Deng Y, Wang Y, Zhou T (2021) Molybdenite Re–Os, titanite and garnet U–Pb dating of the Magushan Skarn Cu–Mo deposit, Xuancheng district, middle–lower Yangtze River Metallogenic Belt. Geosci Front 12:101116. https://doi.org/10.1016/j.gsf.2020.11.013

Lima ESD (1987) Evolução termo-barométrica das rochas metapelíticas da região do Seridó, nordeste brasileiro. Rev Bras Geociências 17:315–323

Lima ES (1992) Metamorphic conditions in the Seridó region of northeastern Brazil during the Brasiliano cycle (late Proterozoic). J South Am Earth Sci 5:265–273. https://doi.org/10.1016/0895-9811(92)90025-T

McInnes BIA (2005) Application of thermochronology to hydrothermal ore deposits. Rev Mineral Geochem 58:467–498. https://doi.org/10.2138/rmg.2005.58.18

Meinert LD, Dipple GM, Nicolescu S (2005) World Skarn deposits. In: Hedenquist JW, Thompson JFH, Goldfarb RJ, Richards JP (eds) One hundredth anniversary volume. Society of Economic Geologists, Littleton, pp 299–236

Nascimento RSC, Sial AN, Pimentel MM (2004) Chemostratigraphy of medium-grade marbles of the late Neoproterozoic Seridó Group, Seridó Fold Belt, Northeastern Brazil. Gondwana Res 7:731–744. https://doi.org/10.1016/S1342-937X(05)71059-5

Nascimento RSC, Sial AN, Pimentel MM (2007) C- and Sr-isotope systematics applied to neoproterozoic marbles of the Seridó Belt, northeastern Brazil. Chem Geol 237:191–210. https://doi.org/10.1016/j.chemgeo.2006.06.017

Nascimento MAL, Galindo AC, Medeiros VC (2015) Ediacaran to Cambrian magmatic suites in the Rio Grande do norte domain, extreme northeastern Borborema Province (NE of Brazil): current knowledge. J South Am Earth Sci 58:281–299. https://doi.org/10.1016/j.jsames.2014.09.008

Newton RC, Charlu TV, Kleppa OJ (1980) Thermochemistry of the high structural state plagioclases. Geochim Cosmochim Acta 44:933–941. https://doi.org/10.1016/0016-7037(80)90283-5

Ohmoto H, Rye RO (1979) Isotope of sulfur and carbon. In: Barnes HL (ed) Geochemistry of hydrothermal deposits, 2nd edn. John Wiley and Sons, Inc., New York, pp 509–567

Oliveira RG, Medeiros WE (2018) Deep crustal framework of the Borborema Province, NE Brazil, derived from gravity and magnetic data. Precambrian Res 315:45–65. https://doi.org/10.1016/j.precamres.2018.07.004

Orhan A, Mutlu H, Fallick AE (2011) Fluid infiltration effects on stable isotope systematics of the Susurluk skarn deposit, NW Turkey. J Asian Earth Sci 40:550–568. https://doi.org/10.1016/j.jseaes.2010.10.009

Putnis A, Austrheim H (2010) Fluid-induced processes: Metasomatism and metamorphism. Geofluids 10:254–269. https://doi.org/10.1111/j.1468-8123.2010.00285.x

Robb LJ (2005) Introduction to ore-forming processes. Blackwell Pub, Malden, MA

Romer RL, Smeds S-A (1994) Implications of U–Pb ages of columbite-tantalites from granitic pegmatites for the Palaeoproterozoic accretion of 1.90–1.85 Ga magmatic arcs to the Baltic Shield. Precambrian Res 67:141–158. https://doi.org/10.1016/0301-9268(94)90008-6

Romer RL, Wright JE (1992) U–Pb dating of columbites: a geochronologic tool to date magmatism and ore deposits. Geochim Cosmochim Acta 56:2137–2142. https://doi.org/10.1016/0016-7037(92)90337-I

Romer RL, Kroner U, Schmidt C, Legler C (2022) Mobilization of tin during continental subduction-accretion processes. Geology 50:1361–1365. https://doi.org/10.1130/G50466.1

Sahlström F, Jonsson E, Högdahl K, Troll VR, Harris C, Jolis EM, Weis F (2019) Interaction between high-temperature magmatic fluids and limestone explains 'Bastnäs-type' REE deposits in central Sweden. Sci Rep 9:15203. https://doi.org/10.1038/s41598-019-49321-8

Sallet R, Ribeiro C, Souza Neto JA, Sales M, Moritz R, Price JD, Thomsen TB (2021) Pegmatitic granite fluid compositions and thermochronometry in the Seridó Belt, Borborema Province, Brazil: insights from trace element advection-diffusion-partitioning halos in host schist and gneiss. Lithos 396–397. https://doi.org/10.1016/j.lithos.2021.106200

Santiago JS, Souza VS, Dantas EL, Oliveira CG (2019) Ediacaran emerald mineralization in Northeastern Brazil: the case of the Fazenda Bonfim Deposit. Braz J Geol 49:e20190081. https://doi.org/10.1590/2317-4889201920190081

Santos EJ, Souza Neto JA, Silva M, Beurlen H, Dias Cavalcanti J, Silva M, Dias V, Costa Á, Santos L, Santos R (2014) Metalogênese das porções norte e central Da Província Borborema. SGB/CPRM, Brasilia, pp 343–388

Sato K, Tassinari CCG, Basei MAS, Siga Júnior O, Onoe AT, Souza MD (2014) Sensitive high resolution Ion Microprobe (SHRIMP IIe/MC) of the Institute of Geosciences of the University of São Paulo, Brazil: Analytical method and first results. Geol USP Série Científica 14:3–18. https://doi.org/10.5327/Z1519-874X201400030001

Sheppard SMF (1981) Stable isotope geochemistry of fluids. Phys Chem Earth 13–14:419–445. https://doi.org/10.1016/0079-1946(81)90021-5

Shin D, Lee I (2003) Evaluation of the volatilization and infiltration effects on the stable isotopic and mineralogical variations in the carbonate rocks adjacent to the cretaceous Muamsa Granite, South Korea. J Asian Earth Sci 22:227–243. https://doi.org/10.1016/S1367-9120(03)00064-6

Sial AN, Campos MS, Gaucher C, Frei R, Ferreira VP, Nascimento RC, Pimentel MM, Pereira NS, Rodler A (2015) Algoma-type neoproterozoic BIFs and related marbles in the Seridó Belt (NE Brazil): REE, C, o, Cr and Sr isotope evidence. J South Am Earth Sci 61:33–52. https://doi.org/10.1016/j.jsames.2015.04.001

Silva DRV, Souza ZS (2012) Petrografia E textura do pluton granitoide pós-colisional Serra Da Macambira, Neoproterozoico Da Província Borborema (nordeste do Brasil). Rev Bras Geociências 42:713–728. https://doi.org/10.5327/Z0375-75362012000400005

Silva MRR, Höll R, Beurlen H (1995) Borborema Pegmatitic Province: geological and geochemical characteristics. J South Am Earth Sci 8:355–364. https://doi.org/10.1016/0895-9811(95)00019-C

Souza LC (1996) Zonéographie Métamorphique, Chimie des Minéraux, Pétrochimie, Géochronologie $^{40}Ar/^{39}Ar$ et Histoire P-T-t des Micaschistes Englobant le Massif Gabbro-Granitique d'Acari (Brasiliano), Ceinture Mobile du Seridó (NE du Brésil). PhD thesis, Universite Catholique de Louvain

Souza LC, Legrand JM, Verkaeren J (2007) Metamorfismo térmico nos micaxistos Seridó em torno do batólito granítico de Acari (RN), Nordeste do Brasil: química mineral de Ilmenitas E turmalinas. Estud Geol 17:71–84

Souza ZS, Kalsbeek F, Deng X-D, Frei R, Kokfelt TF, Dantas EL, Li J-W, Pimentel MM, Galindo AC (2016) Generation of continental crust in the northern part of the Borborema Province, northeastern Brazil, from Archaean to Neoproterozoic. J South Am Earth Sci 68:68–96. https://doi.org/10.1016/j.jsames.2015.10.006

Souza Neto JA, Sonnet P, Legrand JM, Volfinger M, Pascal M-L (1998) Geochemistry of the ore fluids in the Bonfim and Itajubatiba

gold skarn deposits, Northeastern Brazil: a PIXE method study. Mineral Mag 62A:1432–1433. https://doi.org/10.1180/minmag.1998.62A.3.84

Souza Neto JA, Sonnet P, Legrand JM, Melo G Jr. (1999) Bonfim and Itajubatiba gold deposits, NE Brazil: C and O isotope evidence for skarn origin. In: Stanley CJ, Rankin AH, Bodnar R et al (eds) Mineral deposits: processes to processing. Balkema, Rotterdan, pp 1439–1442

Souza Neto JA, Legrand JM, Volfinger M, Pascal M-L, Sonnet P (2008) W–Au skarns in the neo-proterozoic Seridó Mobile Belt, Borborema Province in northeastern Brazil: an overview with emphasis on the Bonfim deposit. Min Deposita 43:185–205. https://doi.org/10.1007/s00126-007-0155-1

Souza Neto JA, Volfinger M, Pascal M-L, Legrand JM, Sonnet P (2012) The occurrence of gold-rich pyrite in the Itajubatiba Skarn deposit, Borborema Province, Northeastern Brazil: a discovery by PIXE analyses. Geociências 31:553–566

Stacey JS, Kramers JD (1975) Approximation of terrestrial lead isotope evolution by a two-stage model. Earth Planet Sci Lett 26:207–221. https://doi.org/10.1016/0012-821X(75)90088-6

Stein HJ, Markey RJ, Morgan JW, Hannah JL, Schersten A (2001) The remarkable re-os chronometer in molybdenite: how and why it works. Terra Nova 13:479–486. https://doi.org/10.1046/j.1365-3121.2001.00395.x

Strmić Palinkaš S, Palinkaš L, Neubauer F et al (2019) Formation conditions and $^{40}Ar/^{39}Ar$ age of the gem-bearing Boqueirão granitic pegmatite, Parelhas, Rio Grande do Norte, Brazil. Minerals 9:233. https://doi.org/10.3390/min9040233

Suzuki K, Shimizu H, Masuda A (1996) Re-os dating of molybdenites from ore deposits in Japan: implication for the closure temperature of the re-os system for molybdenite and the cooling history of molybdenum ore deposits. Geochim Cosmochim Acta 60:3151–3159. https://doi.org/10.1016/0016-7037(96)00164-0

Tajčmanová L, Connolly JAD, Cesare B (2009) A thermodynamic model for titanium and ferric iron solution in biotite. J Metamorph Geol 27:153–165. https://doi.org/10.1111/j.1525-1314.2009.00812.x

Taylor HP (1974) The application of oxygen and hydrogen isotope studies to problems of hydrothermal alteration and ore deposition. Econ Geol 69:843–883. https://doi.org/10.2113/gsecongeo.69.6.843

Taylor HP (1977) Water/rock interactions and the origin of H_2O in granitic batholiths: Thirtieth William Smith lecture. J Geol Soc 133:509–558. https://doi.org/10.1144/gsjgs.133.6.0509

Taylor BE (1986) Magmatic volatiles; isotopic variation of C, H, and S. Rev Mineral Geochem 16:185–225

Taylor BE (1992) Degassing of H_2O from rhyolite magma during eruption and shallow intrusion, and the isotopic composition of magmatic water in hydrothermal systems. In: Hedenquist JK (ed) Magmatic contributions to hydrothermal systems and the behavior of volatiles in magma, Report 279. Geological Survey of Japan, Tokyo, pp 190–194

Timón SM, Moro MC, Cembranos ML, Fernández A, Crespo JL (2007) Contact metamorphism in the Los Santos W Skarn (NW Spain). Mineral Petrol 90:109–140. https://doi.org/10.1007/s00710-006-0166-0

Valley JW (1986) Stable isotope geochemistry of metamorphic rocks. In: Valley JW, Taylor HP, O'Neil JR (eds) Stable isotopes in high temperature geological processes. De Gruyter, Berlin, Boston, pp 445–490

Van Schmus WR, Brito Neves BB, Williams IS, Hackspacher PC, Fetter AH, Dantas EL, Babinski M (2003) The Seridó Group of NE Brazil, a late Neoproterozoic pre- to syn-collisional basin in West Gondwana: insights from SHRIMP U–Pb detrital zircon ages and Sm–Nd crustal residence (TDM) ages. Precambrian Res 127:287–327. https://doi.org/10.1016/S0301-9268(03)00197-9

Van Schmus WR, Kozuch M, Brito Neves BB (2011) Precambrian history of the Zona Transversal of the Borborema Province, NE Brazil: insights from Sm–Nd and U–Pb geochronology. J South Am Earth Sci 31:227–252. https://doi.org/10.1016/j.jsames.2011.02.010

Vauchez A, Neves S, Caby R, Corsini M, Egydio-Silva M, Arthaud M, Amaro V (1995) The Borborema shear zone system, NE Brazil. J South Am Earth Sci 8:247–266. https://doi.org/10.1016/0895-9811(95)00012-5

Vermeesch P (2018) IsoplotR: a free and open toolbox for geochronology. Geosci Front 9:1479–1493. https://doi.org/10.1016/j.gsf.2018.04.001

White RW, Powell R, Holland TJB, Worley BA (2000) The effect of TiO_2 and Fe_2O_3 on metapelitic assemblages at greenschist and amphibolite facies conditions: Mineral equilibria calculations in the system K_2O-FeO-MgO-Al_2O_3-SiO_2-H_2O-TiO_2-Fe_2O_3. J Metamorph Geol 18:497–511. https://doi.org/10.1046/j.1525-1314.2000.00269.x

Zhang T, Zhang D, Danyushevsky LV, Wu M, Koffi Alexis N, Liao Y, Zhang J (2020) Timing of multiple magma events and duration of the hydrothermal system at the Yu'erya gold deposit, eastern Hebei Province, China: constraints from U–Pb and Ar–Ar dating. Ore Geol Rev 127:103804. https://doi.org/10.1016/j.oregeorev.2020.103804

Zharikov VA (1970) Skarns (Part I). Int Geol Rev 12:541–559. https://doi.org/10.1080/00206817009475262

Zheng Y-F (1999) Oxygen isotope fractionation in carbonate and sulfate minerals. Geochem J 33:109–126. https://doi.org/10.2343/geochemj.33.109